Finite volume element-discontinuous Galerkin approximation of viscous two-phase flow in heterogeneous porous media

Raimund Bürger · Sarvesh Kumar · Sudarshan Kumar K. · Ricardo Ruiz-Baier

Received: date / Revised version: date Updated: March 26, 2015

Abstract Runge-Kutta Discontinuous Galerkin (RKDG) and Discontinuous Finite Volume Element (DFVE) methods are applied to a coupled flow-transport problem describing the immiscible displacement of a viscous incompressible fluid in a non-homogeneous porous medium. The model problem consists of a nonlinear pressure-velocity equation assuming Brinkman flow, coupled to a nonlinear hyperbolic equation governing the mass balance (saturation equation). The mass conservation properties inherent to finite volume-based methods motivate a DFVE scheme for the approximation of the Brinkman flow in combination with a RKDG method for the spatio-temporal discretization of the saturation equation. The stability of the scheme for the saturation equation is analyzed. Several numerical experiments illustrate the robustness of the numerical method.

Keywords Two phase flow · Brinkman equations · Discontinuous Galerkin methods · Stabilization · Finite volume element methods

Mathematics Subject Classification (2000) 76S05 · 65M08 · 65M60 · 65M12

1 Introduction

1.1 Scope

It is the primary purpose of this contribution to introduce a new numerical approach for the accurate simulation of two-phase flow (for instance oil and water) in a heterogeneous porous medium. The flow of the mixture is governed by the Brinkman model while the interaction of the two phases can be described by the fractional flow formalism, which translates into a transport equation of one

R. Bürger (Corresponding author)
CI^{2}MA and Departamento de Ingeniería Matemática, Universidad de Concepción, Casilla 160-C, Concepción, Chile
E-mail: rburger@ing-mat.udec.cl

S. Kumar
Department of Mathematics, Indian Institute of Space Science and Technology, Thiruvananthapuram 695 547, Kerala, India
E-mail: sarvesh@iist.ac.in

S. Kumar K.
CI^{2}MA, Universidad de Concepción, Casilla 160-C, Concepción, Chile
E-mail: skumar@ci2ma.udec.cl

R. Ruiz-Baier
Institut des Sciences de la Terre, FGSE, Université de Lausanne, Géopolis Quartier Unil-Mouline, CH-1015 Lausanne, Switzerland
E-mail: ricardo.ruizbaier@unil.ch

phase that involves a nonlinear flux function. Since the medium is considered non-homogeneous, not only the flow properties undergo abrupt changes (as does the permeability of the medium), but also the flux characterization will exhibit discontinuities associated to different nonlinearities adjacent to a discontinuity in the medium.

Specifically, the governing model is defined as follows. Let us consider a mixture of two fluids, a wetting phase and a non-wetting phase (e.g., water and oil) identified by the indices w and n, with saturations $\phi_{\mathrm{w}} = \phi$ and $\phi_{\mathrm{n}} = 1 - \phi$, respectively, in a domain $\Omega \subset \mathbb{R}^2$. If the fluids are incompressible and capillary forces are negligible, then the following model is adequate to describe the viscous motion of the mixture in a porous medium:

$$\partial_t \phi + \operatorname{div} \mathbf{F}(\phi, \boldsymbol{u}, \boldsymbol{x}) = 0 \qquad \text{in } \Omega \times (0,T), \tag{1.1a}$$

$$\mathbf{K}^{-1}(\boldsymbol{x})\boldsymbol{u} - \mathbf{div}\big(\mu(\phi)\boldsymbol{\varepsilon}(\boldsymbol{u}) - p\mathbf{I}\big) - \phi \boldsymbol{g} = \mathbf{0} \qquad \text{in } \Omega \times (0,T), \tag{1.1b}$$

$$\operatorname{div} \boldsymbol{u} = 0 \qquad \text{in } \Omega \times (0,T), \tag{1.1c}$$

supplied with suitable initial and boundary conditions.

The primal unknowns are the volume average flow velocity of the mixture $\boldsymbol{u}$, the saturation ϕ, and the pressure field p. In addition, $\mu(\phi)\boldsymbol{\varepsilon}(\boldsymbol{u}) - p\mathbf{I}$ is the Cauchy stress tensor, $\boldsymbol{\varepsilon}(\boldsymbol{u}) = \frac{1}{2}(\nabla \boldsymbol{u} + \nabla \boldsymbol{u}^{\mathrm{T}})$ is the infinitesimal rate of strain, $\mu = \mu(\phi)$ is the saturation-dependent viscosity,

$$\mathbf{F}(\phi, \boldsymbol{u}, \boldsymbol{x}) = f(\phi)\boldsymbol{u} + b(\phi)\mathbf{K}(\boldsymbol{x})\boldsymbol{g}, \tag{1.2}$$

is a nonlinear flux vector, $\mathbf{K}$ is the permeability tensor of the medium, and $\boldsymbol{g}$ is the gravity acceleration. In addition, f and b are the fractional flow functions that will be specified later.

We assume that $\mathbf{K}$ is symmetric, uniformly bounded and positive definite, and that μ and $\mathbf{K}^{-1}$ satisfy the following:

$$\mu, \mu' \in \mathrm{Lip}(\mathbb{R}_+); \quad \exists \gamma_1, \mu_{\min}, \mu_{\max} > 0 : \ \forall s \in \mathbb{R}_+ : \ \mu_{\min} < \mu(s) < \mu_{\max}, \ |\mu'(s)| \le \gamma_1, \tag{1.3}$$

$$\forall \boldsymbol{x} \in \Omega; \quad \exists\, k_1, k_2 > 0 \text{ such that } 0 < k_1 \le \mathbf{K}^{-1}(x) \le k_2, \tag{1.4}$$

the last inequalities being understood componentwise.

The numerical approximation of system (1.1) calls for advanced techniques capable to accurately capture flux discontinuities, and robust flow solvers that satisfy discrete maximum principles (ϕ must remain bounded between zero and one), deliver divergence-free approximations of velocity, and ensure local mass conservation. It is known that classical methods (e.g. pure upwind finite volumes or primal finite elements and others) are not able to capture the behavior of the flow near the interface and may yield nonphysical solutions, unless some sort of monotonicity-preserving slope limiter or high-order reconstruction is added. Other possible remedies include multi-point flux approximation, high-order DG or other nonconforming methods, phase field models, XFEM, or level set strategies. Regarding the flow equations (in this case, of Brinkman type), we are interested in accurate methods that would permit a natural development of error estimates (therefore associated to finite element formulations), that are mass conservative by construction (therefore related to mixed formulations, or to pure finite volume schemes), and which could easily handle unstructured meshes. These aspects are the prime motivation for proposing Discontinuous Finite Volume Element (DFVE) methods for the approximation of the Brinkman equations (1.1b), (1.1c) and Runge-Kutta Discontinuous Galerkin (RKDG) approximation of the saturation equation (1.1a). The main novelty of this paper is the particular numerical treatment of the two-phase flow equations (1.1) through the implementation of the RKDG scheme together with the DFVE method and presenting the stability analysis. As we have included the effect of gravity and the medium is heterogeneous, the flux function in (1.1a) is non-monotone in ϕ and discontinuous in $\boldsymbol{x}$. These properties require an appropriate choice of the numerical flux in the RKDG formulation. Showing the robustness of numerical results that arise from incorporating the so-called DFLU flux of [2] into the RKDG formulation further adds to the novelty.

1.2 Related work

We recall that the Brinkman model exhibits the advantage that both Stokes and Darcy flows can be represented without imposing interface (e.g. Beavers-Joseph-Saffman) conditions. The latter are not necessarily consistent with mixture theory, and are moreover quite difficult to treat numerically. In fact, several vectorial and scalar Lagrange multipliers need to be incorporated to impose energy conservation, as is done, for instance, in [3,11,24].

The model (1.1) is similar to the continuum-based description of sedimentation and consolidation of suspended particles recently discretized by FVE-related methods [10,33]. In turn, multiscale FVE methods were applied in [20,23] for the simulation of two-phase flow in porous media. An adaptive FVE was proposed in [29] for a steady convection-diffusion-reaction problem. In [8,25] the authors propose and analyze unified DFVE methods for the approximation of Stokes-transport and Darcy-transport problems, respectively; in [10] an axisymmetric sedimentation problem is discretized with a combination of continuous FVE and DFVE for Stokes and a degenerate parabolic equation, continuous FVE-based formulations for coupled Darcy and transport were proven to satisfy discrete maximum principles [21] and applied to Navier-Stokes–transport couplings in [30,33]; and a hybrid mixed FE–DFVE has been recently introduced in [32] for a larger class of multiphase flow in rigid and compliant porous media.

On the other hand, RKDG methods were developed in [15,16,17,18] with the aim of obtaining physically relevant numerical solutions to nonlinear hyperbolic conservation laws. The most attractive features of RKDG methods include high-order accuracy, nonlinear stability, shock capturing, and the capability of handling complicated geometries and boundary conditions. In addition, generalized "slope limiting" techniques for multidimensional conservation laws [15] have also achieved element-wise mass conservation, prevented spurious oscillations, and yielded nonlinear stability of the underlying scheme. More recently, in [35] a related method was proposed that requires the computed RKDG solution in a cell to satisfy additional conservation constraints in adjacent cells. It was shown that the new formulation leads to a CFL condition that is less restrictive than the one of the original RKDG method. For a survey on RKDG methods and related schemes for nonlinear hyperbolic conservation laws we refer to [14].

Focusing on the approximation of discontinuous fluxes, one can find many other competing strategies in the literature that deal either with the pure transport equation or with the coupling with the description of the flow. These include for instance, high order schemes [7], XFEM formulations to capture discontinuities [22], high-order DG discretizations [5], level set methods, phase field schemes [34], multi-point flux approximation methods [13], artificial viscosity [4], and multiresolution-based adaptivity [9].

1.3 Outline of the paper

The remainder of the paper is organized as follows. In Section 2 we collect some preliminaries, including a description of the fractional flow model (Sect. 2.1), a statement of the initial and boundary conditions for (1.1) (Sect. 2.2) and the weak formulation of the initial-boundary value problem (Sect. 2.3). The spatio-temporal discretization, namely the DFVE-RKDG method, is introduced in Section 3, starting with the FVE formulation for the flow equations (1.1b) and (1.1c) (Sect. 3.1). We then introduce the DG spatial discretization of the saturation equation (Sect. 3.3). The latter needs to handle discontinuities in $\mathbf{K}(\boldsymbol{x})$, and therefore in $\mathbf{F}(\phi, \boldsymbol{u}, \boldsymbol{x})$, with respect to $\boldsymbol{x}$, where we assume that the discontinuities are aligned with the edges of the mesh. To this end, we define in Section 3.4 a numerical flux that emerges from the modified Godunov flux reconstruction advanced in [1] for scalar one-dimensional conservation laws with discontinuous flux. By means of suitable quadrature formulas we generate, in Section 3.5, the fully discrete version of the RKDG formulation for (1.1a). Next, in Section 3.6, we recall the limiter for triangular finite elements from [17] that is introduced to prevent oscillations that possibly arise with high-order DG formulations. Section 4 is devoted to the stability analysis of the resulting RKDG scheme for (1.1a), with the result that under a suitable CFL condition that scheme produces numerical approximations that assume values in $[0, 1]$ only, in

agreement with $\phi_{\mathrm{n}} \geq 0$, $\phi_{\mathrm{w}} \geq 0$ and $\phi_{\mathrm{n}} + \phi_{\mathrm{w}} = 1$. In Section 5 numerical examples are presented. Example 1 (Sect. 5.1) is a simple test case with a known exact solution that is used herein to assess the accuracy of the DFVE formulation for continuous fluxes. Example 2 (Sect. 5.2) demonstrates the performance of the coupled DFVE-RKDG scheme for the full problem (1.1) on a porous square, including a straight flux discontinuity. More involved discontinuities arise in Examples 3 (flow in a quarter-five spot with discontinuous relative and absolute permeability) and 4, in which areas of reduced permeability are distributed in a random-wise manner over the whole computational domain. Some conclusions are presented in Section 6.

2 Preliminaries

2.1 Fractional flow model

We assume that the fractional flow functions f and b are given by

$$f(\phi) = \frac{\lambda_{\mathrm{w}}(\phi)}{\lambda_{\mathrm{w}}(\phi) + \lambda_{\mathrm{n}}(\phi)}, \qquad b(\phi) = f(\phi)\lambda_{\mathrm{n}}(\phi)\Delta\rho,$$

where $\lambda_{\mathrm{w}}, \lambda_{\mathrm{n}}$ are the mobilities of the phases given by

$$\lambda_{\mathrm{w}}(\phi) = \frac{K_{\mathrm{w}}(\phi)}{\mu_{\mathrm{w}}}, \quad \lambda_{\mathrm{n}}(\phi) = \frac{K_{\mathrm{n}}(\phi)}{\mu_{\mathrm{n}}},$$

$\Delta\rho = \rho_{\mathrm{n}} - \rho_{\mathrm{w}}$, where ρ_{n} and ρ_{w} are the densities, and K_{w} and K_{n} are the relative permeabilities of phase w and n, respectively.

If the medium is non-homogeneous, for instance due to fractures characterized by sharp localized discontinuities or due to abrupt changes from one rock type to another, then the intrinsic permeability $\mathbf{K}$ and the relative permeabilities K_{w} and K_{n} will typically depend discontinuously on the spatial variable $\boldsymbol{x}$. This assumption implies that the fractional flow functions f and b, and consequently the flux $\mathbf{F}$, will also be discontinuous. In addition, the coupling conditions at the interface between two kinds of media typically consist in prescribing continuity of the normal flux across the interface. However, since the algebraic definitions of the flux as a function of saturation differ to both sides of the interface, the saturation will in general be discontinuous across that interface [22].

2.2 Initial and boundary conditions

The domain boundary is typically disjointly partitioned into a inlet section, outlet and walls $\partial\Omega = \Gamma_{\mathrm{in}} \cup \Gamma_{\mathrm{out}} \cup \Gamma_{\mathrm{wall}}$. System (1.1) is then supplemented with the following set of boundary conditions

$$\begin{array}{llll} \boldsymbol{u} = \boldsymbol{u}_{\mathrm{in}}, & \phi = \phi_{\mathrm{in}}, & \text{on } \Gamma_{\mathrm{in}} \times (0,T), \\ p = p_{\mathrm{out}}, & \mathbf{F}\cdot\boldsymbol{n} = 0, & \text{on } \Gamma_{\mathrm{out}} \times (0,T), \\ \boldsymbol{u}\cdot\boldsymbol{n} = 0, & \mathbf{F}\cdot\boldsymbol{n} = 0, & \text{on } \Gamma_{\mathrm{wall}} \times (0,T) \end{array} \tag{2.1}$$

along with the initial data

$$\boldsymbol{u}(0) = \boldsymbol{u}_0, \quad \phi(0) = \phi_0 \quad \text{on } \Omega \times \{0\}. \tag{2.2}$$

For sake of clarity, instead of using (2.1) we will restrict the presentation to the case of homogeneous Dirichlet data for velocity and saturation on the whole boundary:

$$\boldsymbol{u} = \mathbf{0}, \qquad \phi = 0, \qquad \text{on } \Gamma \times (0,T).$$

2.3 Weak formulation

Multiplying the first and second equation of (1.1) by $\varphi \in \mathbf{H}_0^1(\Omega)$ and $\boldsymbol{v} \in H_0^1(\Omega)$, respectively, and using the Gauss divergence theorem yields the following weak formulation for (1.1):

For $0 < t < T$, find $(\boldsymbol{u}(t), p(t), \phi(t)) \in \mathbf{H}_0^1(\Omega) \times L_0^2(\Omega) \times H_0^1(\Omega)$ such that

$$\begin{aligned}
(\partial_t \phi, \varphi)_\Omega - (\mathbf{F}(\boldsymbol{u}, \phi), \nabla\varphi)_\Omega = 0 \quad & \forall \varphi \in H_0^1(\Omega), \\
a(\boldsymbol{u}, \boldsymbol{v}) + c(\boldsymbol{u}, \boldsymbol{v}; \phi) + b(\boldsymbol{v}, p) - d(\phi, \boldsymbol{v}) = 0 \quad & \forall \boldsymbol{v} \in \mathbf{H}_0^1(\Omega), \\
b(\boldsymbol{u}, q) = 0 \quad & \forall q \in L^2(\Omega), \\
\phi(0) = \phi_0 \quad & \text{a.e. in } \Omega,
\end{aligned}$$

where $\mathbf{H}_0^1(\Omega) := \{\boldsymbol{v} \in \mathbf{H}^1(\Omega) : \boldsymbol{v}|_\Gamma = 0\}$, $L_0^2(\Omega) := \{q \in L^2(\Omega) : \int_\Omega q \,\mathrm{d}\boldsymbol{x} = 0\}$, $H_0^1(\Omega) := \{s \in H^1(\Omega) : s|_\Gamma = 0\}$ and the involved forms are defined as

$$\begin{aligned}
a(\boldsymbol{u}, \boldsymbol{v}) &:= (\mathbf{K}^{-1}(\boldsymbol{x})\boldsymbol{u}, \boldsymbol{v})_\Omega, \quad c(\boldsymbol{u}, \boldsymbol{v}; \phi) = (\mu(\phi)\boldsymbol{\varepsilon}(\boldsymbol{u}), \boldsymbol{\varepsilon}(\boldsymbol{v}))_\Omega, \\
b(\boldsymbol{v}, q) &:= -(q, \operatorname{div} \boldsymbol{v})_\Omega, \quad d(\phi, \boldsymbol{v}) := (\phi \boldsymbol{g}, \boldsymbol{v})_\Omega.
\end{aligned}$$

The existence of weak solutions to this problem was recently established in [19].

3 Spatio-temporal discretization

3.1 Finite volume element formulation for the flow equations

Let $\mathcal{T}_h$ be a regular, quasi-uniform partition of the domain Ω formed by closed triangles. For each triangular element K, we denote by ∂K and h_K its boundary and diameter, respectively. Each face σ between two neighboring elements K and L has diameter h_σ. The set of all faces in $\mathcal{T}_h$ is denoted by $\mathcal{E}_h$, $\mathcal{E}_h^\Gamma$ is its restriction to boundary faces, and s_j, $j = 1, \ldots, N_h$, are the vertices of triangular mesh. Corresponding to the primal mesh $\mathcal{T}_h$ we also define the dual mesh $\mathcal{T}_h^\sharp$ consisting of all sub-triangles (denoted D_σ) obtained as follows: we divide each triangle $K \in \mathcal{T}_h$ into three sub-triangles by connecting the barycenter of each original triangle to the vertices of that triangle, see the construction in [27].

Now, let $\boldsymbol{n}_{K,\sigma}$ denote the outward vector of $K \in \mathcal{T}_h$ normal to $\sigma \subset \partial K$. For a scalar function $q \in L^2(\Omega)$ we let $[\![q]\!]_\sigma := q|_K - q|_L$ denote a scalar jump across $\sigma = \bar{K} \cap \bar{L}$ and

$$[\![q\boldsymbol{n}_{K,\sigma}]\!]_\sigma := q|_{\partial K}\boldsymbol{n}_{K,\sigma} - q|_{\partial L}\boldsymbol{n}_{L,\sigma}$$

denotes a vector jump across σ. By $\{q\}_\sigma$ we denote its average value on σ. If $\sigma \in \mathcal{E}_h^\Gamma$, then we simply consider $[\![q]\!]_\sigma = \{q\}_\sigma = q|_\sigma$. For $\boldsymbol{v}_h \in \boldsymbol{\mathcal{V}}_h$ we denote by $[\![\boldsymbol{v}_h]\!]_\sigma = \boldsymbol{v}_h|_K - \boldsymbol{v}_h|_L$ and $\{\boldsymbol{v}_h\}_\sigma = \frac{1}{2}(\boldsymbol{v}_h|_K + \boldsymbol{v}_h|_L)$ its jump and average across σ, respectively.

Moreover, let $\mathbb{P}_n(K)$ be the set of all real polynomials of degree less or equal n over the element K and $h = \max_{K \in \mathcal{T}_h}(h_K)$ be the meshsize of the mesh $\mathcal{T}_h$. We define the following trial finite-dimensional subspaces for velocity $\boldsymbol{u}$ and pressure p on a triangular mesh:

$$\boldsymbol{\mathcal{V}}_h := \big\{\boldsymbol{v} \in \mathbf{L}^2(\Omega) : \boldsymbol{v}|_K \in \mathbb{P}_1(K)^2 \,\forall K \in \mathcal{T}_h\big\}, \;\; \mathcal{Q}_h := \big\{q \in L_0^2(\Omega) : q|_K \in \mathbb{P}_0(K) \,\forall K \in \mathcal{T}_h\big\}.$$

The test space for velocity on the dual mesh is defined as

$$\boldsymbol{\mathcal{V}}_h^\sharp := \big\{\boldsymbol{v} \in \mathbf{L}^2(\Omega) : \boldsymbol{v}|_{D_\sigma} \in \mathbb{P}_0(D_\sigma)^2 \,\forall D_\sigma \in \mathcal{T}_h^\sharp\big\}.$$

Define $\boldsymbol{\mathcal{V}}(h) := \boldsymbol{\mathcal{V}}_h + (\mathbf{H}^2(\Omega) \cap \mathbf{H}_0^1(\Omega))$. To connect $\boldsymbol{\mathcal{V}}(h)$ to $\boldsymbol{\mathcal{V}}_h^\sharp$ we define the projection map $\boldsymbol{\mathcal{P}}^\sharp : \boldsymbol{\mathcal{V}}_h \to \boldsymbol{\mathcal{V}}_h^\sharp$ as follows:

$$\boldsymbol{\mathcal{P}}^\sharp \boldsymbol{v}|_{D_\sigma} = \frac{1}{h_\sigma} \int_\sigma \boldsymbol{v}|_{D_\sigma} \,\mathrm{d}s.$$

Applying the Cauchy-Schwarz inequality, we obtain

$$[\![\boldsymbol{\mathcal{P}}^\sharp \boldsymbol{v}_h]\!]_\sigma^2 = h_\sigma^{-2}\left(\int_\sigma [\![\boldsymbol{v}_h]\!]_\sigma \,\mathrm{d}s\right)^2 \,\mathrm{d}s \le h_\sigma^{-2}\left(\int_\sigma \mathrm{d}s\right)\left(\int_\sigma [\![\boldsymbol{v}_h]\!]_\sigma^2 \,\mathrm{d}s\right) = h_\sigma^{-1}\int_\sigma [\![\boldsymbol{v}_h]\!]_\sigma^2 \,\mathrm{d}s. \tag{3.1}$$

Moreover, we note that the projection operator $\boldsymbol{\mathcal{P}}^\sharp$ is self-adjoint with respect to the L^2-inner product, i.e.,

$$(\boldsymbol{v}_h, \boldsymbol{\mathcal{P}}^\sharp \boldsymbol{u}_h) = (\boldsymbol{u}_h, \boldsymbol{\mathcal{P}}^\sharp \boldsymbol{v}_h) \quad \forall \boldsymbol{u}_h, \boldsymbol{v}_h \in \boldsymbol{\mathcal{V}}_h. \tag{3.2}$$

A proof of the scalar version of (3.2) is given in [6, pp. 373]. Moreover, if we define $|||\boldsymbol{v}_h|||_0 := (\boldsymbol{v}_h, \boldsymbol{\mathcal{P}}^\sharp \boldsymbol{v}_h)$, then $\|\cdot\|_{0,\Omega}$ and $|||\cdot|||_0$ are equivalent (see [25]), i.e., there exist positive constants C_1 and C_2 independent of h such that

$$C_1|||\boldsymbol{v}_h|||_0 \le \|\boldsymbol{v}_h\|_{0,\Omega} \le C_2|||\boldsymbol{v}_h|||_0 \quad \forall \boldsymbol{v}_h \in \boldsymbol{\mathcal{V}}_h. \tag{3.3}$$

In addition, using the construction properties of the diamond mesh and simple calculations provide the following technical lemma, which deals with properties of the transfer operator $\boldsymbol{\mathcal{P}}^\sharp$ (see proofs in e.g. [25,26]):

Lemma 1 *Let $\boldsymbol{v}_h \in \boldsymbol{\mathcal{V}}_h$, $K \in \mathcal{T}_h$ and $\sigma \subset \partial K$. Then the following properties are satisfied:*

$$\int_K (\boldsymbol{v}_h - \boldsymbol{\mathcal{P}}^\sharp \boldsymbol{v}_h)\,\mathrm{d}s = 0, \quad \int_\sigma (\boldsymbol{v}_h - \boldsymbol{\mathcal{P}}^\sharp \boldsymbol{v}_h)\,\mathrm{d}s = 0, \quad \|\boldsymbol{\mathcal{P}}^\sharp \boldsymbol{v}_h\|_{0,\Omega} = \|\boldsymbol{v}_h\|_{0,\Omega} \tag{3.4}$$
$$\left\|\boldsymbol{v}_h - \boldsymbol{\mathcal{P}}^\sharp \boldsymbol{v}_h\right\|_{0,K} \le Ch_K|\boldsymbol{v}_h|_{1,K}, \quad [\![\boldsymbol{v}_h]\!]_\sigma = \boldsymbol{0} \Rightarrow [\![\boldsymbol{\mathcal{P}}^\sharp \boldsymbol{v}_h]\!]_\sigma = \boldsymbol{0}.$$

Multiplying the first and third equations of (1.1) by $\boldsymbol{\xi}_h \in \boldsymbol{\mathcal{V}}_h^\sharp$ and $q_h \in \mathcal{Q}_h$, respectively, using the Gauss divergence theorem on each dual element D_σ and employing the fact that the exact solutions $(\boldsymbol{u}, p)$ satisfy $[\![\boldsymbol{\varepsilon}(\boldsymbol{u})\boldsymbol{n}]\!]_\sigma = \boldsymbol{0}$ and $[\![p\boldsymbol{n}]\!]_\sigma = \boldsymbol{0}$ on every $\sigma \in \mathcal{E}_h^{\mathrm{int}}$, we arrive at the following variational formulation (see also [36]):

Find $\boldsymbol{u} \in \mathbf{H}_0^1(\Omega)$ and $p \in L_0^2(\Omega)$ such that

$$a(\boldsymbol{u}, \boldsymbol{\xi}_h) + c_0(\boldsymbol{u}, \boldsymbol{\xi}_h; \phi) + b_0(\boldsymbol{\xi}_h, p) - d(\phi, \boldsymbol{\xi}_h) = 0 \quad \forall \boldsymbol{\xi}_h \in \boldsymbol{\mathcal{V}}_h^\sharp, \tag{3.5}$$
$$b(\boldsymbol{u}, q_h) = 0 \quad \forall q_h \in \mathcal{Q}_h, \tag{3.6}$$

where we define

$$c_0(\boldsymbol{u}, \xi_{\mathbf{h}}; \phi) := -\sum_{K\in\mathcal{T}_h}\sum_{j=1}^{d+1}\int_{s_{j+1}b_K s_j} \mu(\phi)\boldsymbol{\varepsilon}(\boldsymbol{u})\boldsymbol{n}\cdot\boldsymbol{\xi}_h \,\mathrm{d}s - \sum_{\sigma\in\mathcal{E}_h}\int_\sigma \{\mu(\phi)\boldsymbol{\varepsilon}(\boldsymbol{u})\boldsymbol{n}\}_\sigma \cdot [\![\boldsymbol{\xi}_h]\!]_\sigma \,\mathrm{d}s,$$
$$b_0(\boldsymbol{\xi}_h, p) := \sum_{K\in\mathcal{T}_h}\sum_{j=1}^{d+1}\int_{s_{j+1}b_K s_j} p\boldsymbol{n}\cdot\boldsymbol{\xi}_h \,\mathrm{d}s + \sum_{\sigma\in\mathcal{E}_h}\int_\sigma \{p\}_\sigma [\![\boldsymbol{\xi}_h]\!]_\sigma \,\mathrm{d}s.$$

Now, with the help of (3.5) and (3.6), we define the DFVE scheme for the flow equation as follows:

Find $\boldsymbol{u}_h \in \boldsymbol{\mathcal{V}}_h$ and $p_h \in \mathcal{Q}_h$ such that

$$a_h(\boldsymbol{u}_h, \boldsymbol{v}_h) + c_h(\boldsymbol{u}_h, \boldsymbol{v}_h; \phi_h) + C_h(\boldsymbol{v}_h, p_h) - d(\phi_h, \boldsymbol{v}_h) = 0 \quad \forall \boldsymbol{v}_h \in \boldsymbol{\mathcal{V}}_h, \tag{3.7}$$
$$B_h(\boldsymbol{u}_h, q_h) = 0 \quad \forall q_h \in \mathcal{Q}_h, \tag{3.8}$$

where we define for all $\boldsymbol{w}_h, \boldsymbol{v}_h \in \boldsymbol{\mathcal{V}}_h$ and $r_h, q_h \in \mathcal{Q}_h$

$$a_h(\boldsymbol{w}_h, \boldsymbol{v}_h) := \left(\mathbf{K}^{-1}(\boldsymbol{x})\boldsymbol{w}_h, \boldsymbol{\mathcal{P}}^\sharp \boldsymbol{v}_h\right)_\Omega,$$
$$c_h(\boldsymbol{w}_h, \boldsymbol{v}_h; \phi_h) := -\sum_{K\in\mathcal{T}_h}\sum_{j=1}^{d+1}\int_{s_{j+1}b_K s_j} \mu(\phi_h)\boldsymbol{\varepsilon}(\boldsymbol{w}_h)\boldsymbol{n}\cdot\boldsymbol{v}_h \,\mathrm{d}s$$
$$- \sum_{\sigma\in\mathcal{E}_h}\int_\sigma \{\mu(\phi_h)\boldsymbol{\varepsilon}(\boldsymbol{w}_h)\boldsymbol{n}\}_\sigma \cdot [\![\boldsymbol{\mathcal{P}}^\sharp \boldsymbol{v}_h]\!]_\sigma \,\mathrm{d}s - \sum_{\sigma\in\mathcal{E}_h}\int_\sigma \{\mu(\phi_h)\boldsymbol{\varepsilon}(\boldsymbol{v}_h)\boldsymbol{n}\}_\sigma \cdot [\![\boldsymbol{\mathcal{P}}^\sharp \boldsymbol{w}_h]\!]_\sigma \,\mathrm{d}s$$

$$+\sum_{\sigma\in\mathcal{E}_h}\int_\sigma \frac{\alpha_d}{h_\sigma}[\![\boldsymbol{w}_h]\!]_\sigma\cdot[\![\boldsymbol{v}_h]\!]_\sigma\,\mathrm{d}s,$$

$$C_h(\boldsymbol{v}_h,r_h):=\sum_{K\in\mathcal{T}_h}\sum_{j=1}^{d+1}\int_{s_{j+1}b_Ks_j} r_h\boldsymbol{n}\cdot\boldsymbol{\mathcal{P}}^\sharp\boldsymbol{v}_h\,\mathrm{d}s+\sum_{\sigma\in\mathcal{E}_h}\int_\sigma\{r_h\}_\sigma[\![\boldsymbol{v}_h]\!]_\sigma\,\mathrm{d}s,$$

$$B_h(\boldsymbol{w}_h,q_h):=b(\boldsymbol{w}_h,q_h)-\sum_{\sigma\in\mathcal{E}_h}\int_\sigma\{q_h\}_\sigma[\![\boldsymbol{w}_h]\!]_\sigma\,\mathrm{d}s,$$

where α_d is the penalty parameter to be determined at a later stage. Now using the definition of $a_h(\cdot,\cdot)$, (1.4) and (3.3), we see that there exists a positive constant C independent of h such that

$$a_h(\boldsymbol{v}_h,\boldsymbol{v}_h)\geq C\|\boldsymbol{v}_h\|^2_{0,\Omega}. \tag{3.9}$$

For our future analysis we also define the following natural mesh-dependent norms for all $\boldsymbol{v}_h\in\boldsymbol{\mathcal{V}}(h)$:

$$\|\boldsymbol{v}_h\|_h^2:=\sum_{K\in\mathcal{T}_h}|\boldsymbol{v}_h|^2_{1,K}+\sum_{\sigma\in\mathcal{E}_h}h_\sigma^{-1}\,\|[\![\boldsymbol{v}_h]\!]_\sigma\|^2_{0,\sigma}\,,\quad \|\boldsymbol{v}_h\|^2_{1,h}:=\|\boldsymbol{v}_h\|_h^2+\sum_{K\in\mathcal{T}_h}h_K^2|\boldsymbol{v}_h|^2_{2,K}.$$

An application of the standard inverse inequality yields

$$\|\boldsymbol{v}_h\|_{1,h}\leq C\,\|\boldsymbol{v}_h\|_h\quad\forall\boldsymbol{v}_h\in\boldsymbol{\mathcal{V}}_h. \tag{3.10}$$

The following inequality has been proved in [36]:

$$\|\boldsymbol{v}_h\|^2_{0,\Omega}\leq C\left[\sum_{K\in\mathcal{T}_h}|\boldsymbol{v}_h|^2_{1,K}+\sum_{\sigma\in\mathcal{E}_h}[\![\boldsymbol{\mathcal{P}}^\sharp\boldsymbol{v}_h]\!]^2_\sigma+\sum_{K\in\mathcal{T}_h}h_K^2|\boldsymbol{v}_h|^2_{2,K}\right]\quad\forall\boldsymbol{v}_h\in\boldsymbol{\mathcal{V}}_h.$$

Therefore, by employing (3.1) and (3.10), we have the following discrete Poincaré-Friedrichs type inequality

$$\|\boldsymbol{v}_h\|_{0,\Omega}\leq C\,\|\boldsymbol{v}_h\|_h\qquad\forall\boldsymbol{v}_h\in\boldsymbol{\mathcal{V}}_h, \tag{3.11}$$

where C is independent of h. We also note that for a given ϕ_h, the bilinear form $c_h(\cdot,\cdot;\phi_h)$ will be coercive with respect to $\|\cdot\|_h$, see [8], i.e., there exists a constant α independent of h such that

$$c_h(\boldsymbol{v}_h,\boldsymbol{v}_h;\phi_h)\geq\alpha\,\|\boldsymbol{v}_h\|_h^2\,. \tag{3.12}$$

Moreover, the choices of the finite dimensional spaces $\boldsymbol{\mathcal{V}}_h$ and $\mathcal{Q}_h$ satisfy the following inf-sup condition (see [36]):

$$\sup_{\boldsymbol{v}_h\in\boldsymbol{\mathcal{V}}_h}\frac{B_h(\boldsymbol{v}_h,q_h)}{\|\boldsymbol{v}_h\|_h}\geq\beta_1\|q_h\|_{0,\Omega}, \tag{3.13}$$

where $\beta_1>0$ is independent of h. An application of the Gauss divergence theorem and (3.1) provide the following relationship between the bilinear forms $B_h(\cdot,\cdot)$ and $C_h(\cdot,\cdot)$ and will be used for deriving error estimates for velocity and pressure; for a proof, see [36].

Lemma 2 *For all $\boldsymbol{v}\in\boldsymbol{\mathcal{V}}(h)$, we have*

$$C_h(\boldsymbol{v},q_h)=-B_h(\boldsymbol{v},q_h)\quad\forall q_h\in\mathcal{Q}_h. \tag{3.14}$$

Moreover, $C_h(\cdot,\cdot)$ is bounded in the following sense:

$$|C_h(\boldsymbol{v},q)|\leq C\,\|\boldsymbol{v}\|_{1,h}\left[\|q\|_{0,\Omega}+\left(\sum_K h_K^2|q|^2_{1,K}\right)^{1/2}\right]\quad\forall\boldsymbol{v}\in\boldsymbol{\mathcal{V}}(h),\quad q\in L^2_0(\Omega). \tag{3.15}$$

3.2 Error estimates for velocity and pressure

In order to derive the estimates for $\boldsymbol{u}$ and p, by following [36], we define the mapping $\pi_K : H^1(K) \longrightarrow P_1(K)$ that satisfies

$$\int_{\sigma_j} \pi_K v \, \mathrm{d}s = \int_{\sigma_j} v \, \mathrm{d}s \quad \forall \boldsymbol{v} \in H^1(K), \quad j = 1, 2, 3,$$

where σ_j, $j = 1, 2, 3$ are three edges of the triangle K. Also, the operator π_K satisfies the following approximation properties (see [31])

$$|\pi_K v - v|_{s,K} \leq C h^{2-s} |\boldsymbol{v}|_{2,K} \quad \forall v \in H^2(K), \quad s = 0, 1, 2. \tag{3.16}$$

Then the projection map $\mathbf{I}_h : \mathbf{H}_0^1(\Omega) \longrightarrow \boldsymbol{\mathcal{V}}_h$ defined by $(\mathbf{I}_h \boldsymbol{v})_i|_K = \pi_K v_i \;\; i = 1, 2$ satisfies (see [36]):

$$B(\boldsymbol{u} - \mathbf{I}_h \boldsymbol{u}, q_h) = 0 \quad \forall q_h \in \mathcal{Q}_h. \tag{3.17}$$

Moreover, by using the definition of $\|\cdot\|_h$ and (3.16), it is easy to see that $\mathbf{I}_h$ has the following approximation property:

$$\|\boldsymbol{u} - \mathbf{I}_h \boldsymbol{u}\|_h \leq C h \|u\|_{2,\Omega}, \tag{3.18}$$

$$\|\boldsymbol{u} - \mathbf{I}_h \boldsymbol{u}\|_{0,\Omega} \leq C h^2 \|u\|_{2,\Omega}. \tag{3.19}$$

Also, let Π_h be the L^2 projection from $L_0^2(\Omega)$ to $\mathcal{Q}_h$ satisfying

$$\|p - \Pi_h p\|_{0,\Omega} \leq C h \|p\|_{1,\Omega}. \tag{3.20}$$

Since the saturation ϕ appears in the pressure-velocity equation (1.1b), the following lemma shows that the error estimates of p and $\boldsymbol{u}$ depend on the estimates of ϕ.

Lemma 3 *Let $(\boldsymbol{u}, p)$ and $(\boldsymbol{u}_h, p_h)$ be the solutions (3.5), (3.6) and (3.7), (3.8), respectively. Then there exists a constant C independent of h, but which may depend on the bound of $\boldsymbol{u}$, such that*

$$\begin{aligned} &\|\boldsymbol{u} - \boldsymbol{u}_h\|_h + \|p - p_h\|_{0,\Omega} \\ &\leq C \left[h\big(\|\boldsymbol{u}\|_{2,\Omega} + \|p\|_{1,\Omega}\big) + \|\phi - \phi_h\|_{0,\Omega} + h \left(\sum_K \|\nabla(\phi - \phi_h)\|_{0,K}^2 \right)^{1/2} \right]. \end{aligned}$$

Proof. Write $\boldsymbol{u} - \boldsymbol{u}_h = \eta + \eta_h$ and $p - p_h = \xi + \xi_h$, where $\eta := \boldsymbol{u} - \mathbf{I}_h \boldsymbol{u}$, $\eta_h := \mathbf{I}_h \boldsymbol{u} - \boldsymbol{u}_h$, $\xi := p - \Pi_h p$ and $\xi_h := \Pi_h p - p_h$. Since estimates for η and ξ are known, it is enough to find the estimates of η_h and ξ_h.

First we note that from (3.5)-(3.6), $(\boldsymbol{u}, p)$ satisfies the following:

$$a_h(\boldsymbol{u}, \boldsymbol{v}_h) + c_h(\boldsymbol{u}, \boldsymbol{v}_h; \phi) + C_h(\boldsymbol{v}_h, p) = d(\phi, \boldsymbol{v}_h) \quad \forall \boldsymbol{v}_h \in \boldsymbol{\mathcal{V}}_h, \tag{3.21}$$

$$B_h(\boldsymbol{u}, q_h) = 0 \quad \forall q_h \in \mathcal{Q}_h. \tag{3.22}$$

Subtracting (3.21) from (3.7) and (3.22) from (3.8), respectively, and using (3.17), we arrive at

$$\begin{aligned} a_h(\eta_h, \boldsymbol{v}_h) + c_h(\eta_h, \boldsymbol{v}_h; \phi_h) + C_h(\boldsymbol{v}_h, \xi_h) &= d(\phi, \boldsymbol{v}_h) - d(\phi_h, \boldsymbol{v}_h) - C_h(\boldsymbol{v}_h, \xi) - a_h(\eta, \boldsymbol{v}_h) \\ &\quad - (c_h(\boldsymbol{u}, \boldsymbol{v}_h; \phi) - c_h(\boldsymbol{u}, \boldsymbol{v}_h; \phi_h)) \quad \forall \boldsymbol{v}_h \in \boldsymbol{\mathcal{V}}_h, \\ B_h(\eta_h, q_h) &= 0 \quad \forall q_h \in \mathcal{Q}_h. \end{aligned} \tag{3.23}$$

Choosing $\boldsymbol{v}_h = \eta_h$ and employing (3.14), we deduce that

$$C_h(\eta_h, \xi_h) = 0.$$

Therefore, using (3.9) and (3.12), we obtain following from (3.23)

$$\|\eta_h\|_h^2 \leq C \left[(d(\phi, \eta_h) - d(\phi_h, \eta_h)) - a_h(\eta, \eta_h) - (c_h(\boldsymbol{u}, \eta_h; \phi) - c_h(\boldsymbol{u}, \eta_h; \phi_h)) - C_h(\eta_h, \xi) \right] \tag{3.24}$$

Note that using definition of $d(\cdot,\cdot)$, the Cauchy-Schwarz inequality, (3.4) and (3.11), we immediately have

$$|d(\phi,\eta_h) - d(\phi_h,\eta_h)| \leq C\|\phi-\phi_h\|_{0,\Omega}\,\|\eta_h\|_h\,. \tag{3.25}$$

Again an application of the Cauchy-Schwarz inequality together with (3.4), (3.11) and (3.19) allows us to write

$$|a_h(\eta,\eta_h)| \leq \|\eta\|_{0,\Omega}\,\|\eta_h\|_h \leq Ch^2\|\boldsymbol{u}\|_{2,\Omega}\,\|\eta_h\|_h\,. \tag{3.26}$$

In light of the assumptions on the viscosity function $\mu = \mu(\phi)$ given in (1.3) and using the same arguments used in the derivation of Lemma 4.3 of [8], the following bound can be easily obtained:

$$|c_h(\boldsymbol{u},\eta_h;\phi) - c_h(\boldsymbol{u},\eta_h;\phi_h)| \leq C\left[\|\phi-\phi_h\|_{0,\Omega} + h\left(\sum_{K\in\mathcal{T}_h}\|\nabla(\phi-\phi_h)\|_{0,K}^2\right)^{1/2}\right]\|\eta_h\|_h\,. \tag{3.27}$$

The following bound directly follows from (3.15), (3.10) and by definition of Π_h:

$$|C_h(\eta_h,\xi)| \leq Ch\,\|\eta_h\|_h\,\|p\|_{1,\Omega}. \tag{3.28}$$

Combining all the bounds derived in (3.24)–(3.28), we obtain from (3.24):

$$\|\eta_h\|_h \leq C\left[\|\phi-\phi_h\|_{0,\Omega} + h\left(\sum_{K\in\mathcal{T}_h}\|\nabla(\phi-\phi_h)\|_{0,K}^2\right)^{1/2} + h(\|\boldsymbol{u}\|_{2,\Omega} + \|p\|_{1,\Omega})\right].$$

For estimating ξ_h we proceed as follows: We choose $\boldsymbol{v}_h = \eta_h$ in (3.23), use (3.9), (3.12) and bounds obtained in (3.24)-(3.28), to arrive at

$$C_h(\eta_h,\xi_h) \leq C\left[\|\phi-\phi_h\|_{0,\Omega} + h\left(\sum_{K\in\mathcal{T}_h}\|\nabla(\phi-\phi_h)\|_{0,K}^2\right)^{1/2} + h(\|\boldsymbol{u}\|_{2,\Omega} + \|p\|_{1,\Omega})\right]\|\eta_h\|_h$$

Now, an application of inf-sup condition (3.13) together with (3.14) yields

$$\|\xi_h\|_{0,\Omega} \leq C\left[\|\phi-\phi_h\|_{0,\Omega} + h\left(\sum_{K\in\mathcal{T}_h}\|\nabla(\phi-\phi_h)\|_{0,K}^2\right)^{1/2} + h(\|\boldsymbol{u}\|_{2,\Omega} + \|p\|_{1,\Omega})\right].$$

Using (3.18) and (3.20), we complete the rest of the proof. ∎

Remark 1 The convergence analysis for the approximated saturation ϕ_h for this particular problem still remains as an open question. However it is uniformly bounded as we show in §4. Together with these stability results and the regularity assumption on saturation, Lemma 3 suggests that a fixed-point iteration between the approximation of the Brinkman and the transport problems is applied on discrete quantities whose discretization error remains uniformly bounded.

3.3 DG spatial discretization of the saturation equation

We assume that each element K can be mapped to a fixed reference element $\hat{K}$ using the operator $T_K : \hat{K} \to K$. In the special case of triangular elements, we will consider the space

$$S_h^k := \left\{s \in H_0^1(\Omega) : s|_K \in \mathbb{P}_k(K) \quad \forall K \in \mathcal{T}_h\right\},$$

where $\mathbb{P}_k(K)$ stands for the space spanned by polynomials of degree at most k, defined on the element K.

Next, let us suppose that the approximate velocity field $\boldsymbol{u}_h$ has been computed previously on the primal mesh. We proceed to multiply the first equation in (1.1) by $s_h \in S_h^k$, integrate by parts over $K \in \mathcal{T}_h$, and replace the exact solution ϕ by its approximation $\phi_h \in S_h^k$ to obtain

$$\begin{aligned} &\frac{\mathrm{d}}{\mathrm{d}t}\big(\phi_h(\boldsymbol{x},t), s_h(\boldsymbol{x})\big)_K - \big(\mathbf{F}(\phi_h(\boldsymbol{x},t), \boldsymbol{u}_h, \boldsymbol{x}), \nabla s_h(\boldsymbol{x})\big)_K \\ &+ \sum_{e\in\partial K} \big\langle \mathbf{F}(\phi_h(\boldsymbol{x},t), \boldsymbol{u}_h, \boldsymbol{x})\cdot \boldsymbol{n}_{e,K}, s_h(\boldsymbol{x})\big\rangle_e = 0 \quad \forall s_h \in S_h^k, \end{aligned} \tag{3.29}$$

where $\boldsymbol{n}_e$ is the unit outward normal to the edge (or face) e. The term $\mathbf{F}(\phi_h(\boldsymbol{x},t), \boldsymbol{u}_h, \boldsymbol{x})\cdot \boldsymbol{n}_{e,K}$ has to be specified appropriately, since $\phi_h(\boldsymbol{x},t)$ is not necessarily continuous across the element boundary. Here, this flux function is approximated following [15], that is, we employ

$$\mathbf{F}(\phi_h(\boldsymbol{x},t), \boldsymbol{u}_h, \boldsymbol{x})\cdot \boldsymbol{n}_{e,K} \approx h\big(\phi_h(\boldsymbol{x}^{\mathrm{int}(K)},t), \phi_h(\boldsymbol{x}^{\mathrm{ext}(K)},t), \boldsymbol{u}_h^e, \boldsymbol{x}, \boldsymbol{n}_e\big),$$

and therefore (3.29) now reads

$$\begin{aligned} &\frac{\mathrm{d}}{\mathrm{d}t}\big(\phi_h(\boldsymbol{x},t), s_h(\boldsymbol{x})\big)_K - \big(\mathbf{F}(\phi_h(\boldsymbol{x},t), \boldsymbol{u}_h, \boldsymbol{x}), \nabla s_h(\boldsymbol{x})\big)_K \\ &+ \sum_{e\in\partial K} \big\langle h\big(\phi_h(\boldsymbol{x}^{\mathrm{int}(K)},t), \phi_h(\boldsymbol{x}^{\mathrm{ext}(K)},t), \boldsymbol{u}_h^e, \boldsymbol{x}, \boldsymbol{n}_e\big), s_h(\boldsymbol{x})\big\rangle_e = 0 \quad \forall s_h \in S_h^k. \end{aligned} \tag{3.30}$$

The volume and face integrals involved in the inner products are computed employing the following quadrature rules, where the nodes $x_{K_j} \in K$ and corresponding weights $\bar{\omega}_j$, $j = 1,\dots,M$, and the nodes $x_{i,e} \in e$ and corresponding weights ω_i, $i = 1,\dots,N$, are specified later:

$$\begin{aligned} &\big(\mathbf{F}(\phi_h(\boldsymbol{x},t), \boldsymbol{u}_h, \boldsymbol{x}), \nabla s_h(\boldsymbol{x})\big)_K \approx \sum_{j=1}^{M} \bar{\omega}_j \mathbf{F}\big(\phi_h(\boldsymbol{x}_{K_j},t), \boldsymbol{u}_h(\boldsymbol{x}_{K_j}), \boldsymbol{x}_{K_j}\big)\cdot \nabla s_h(\boldsymbol{x}_{K_j})|K|, \\ &\big\langle h\big(\phi_h(\boldsymbol{x}^{\mathrm{int}(K)},t), \phi_h(\boldsymbol{x}^{\mathrm{ext}(K)},t), \boldsymbol{u}_h^e, \boldsymbol{x}, \boldsymbol{n}_e\big), s_h(\boldsymbol{x})\big\rangle_e \\ &\approx \sum_{i=1}^{N} \omega_i h\big(\phi_h(\boldsymbol{x}_{i,e}^{\mathrm{int}(K)},t), \phi_h(\boldsymbol{x}_{i,e}^{\mathrm{ext}(K)},t), \boldsymbol{u}_h^e, \boldsymbol{x}_{i,e}, \boldsymbol{n}_e\big) s_h(\boldsymbol{x}_{i,e})|e|, \end{aligned}$$

The corresponding weak formulation (3.30) is then replaced by

$$\begin{aligned} &\frac{\mathrm{d}}{\mathrm{d}t}\big(\phi_h(\boldsymbol{x},t), s_h(\boldsymbol{x})\big)_K - \sum_{j=1}^{M} \bar{\omega}_j \mathbf{F}\big(\phi_h(\boldsymbol{x}_{K_j},t), \boldsymbol{u}_h(\boldsymbol{x}_{K_j}), \boldsymbol{x}_{K_j}\big)\cdot \nabla s_h(\boldsymbol{x}_{K_j})|K| \\ &+ \sum_{e\in\partial K}\sum_{i=1}^{N} \omega_i h\big(\phi_h(\boldsymbol{x}_{i,e}^{\mathrm{int}(K)},t), \phi_h(\boldsymbol{x}_{i,e}^{\mathrm{ext}(K)},t), \boldsymbol{u}_h^e, \boldsymbol{x}_{i,e}, \boldsymbol{n}_e\big) s_h(\boldsymbol{x}_{i,e})|e| = 0 \quad \forall s_h \in S_h^k. \end{aligned} \tag{3.31}$$

3.4 Properties of the numerical flux

To motivate the definition of the numerical flux, we assume for the moment that the flux vector $\mathbf{F}$ does not depend on $\boldsymbol{x}$. Let us write $\mathbf{F} = (F_1, F_2)$, $\boldsymbol{n} = (n_1, n_2)$. Moreover, we assume that both flux components F_1 and F_2 are functions of only saturation variable ϕ and are convex. We define

$$\tilde{h}(\alpha,\beta,\boldsymbol{n}) := \hat{F}_1(\alpha,\beta,n_1) + \hat{F}_2(\alpha,\beta,n_2), \tag{3.32}$$

and notice that depending on the normal directions, the components of the numerical flux $\hat{F}_1$ and $\hat{F}_2$ can be computed as follows (we use the notation $F_i n_1(\cdot) = F_i(\cdot)n_1$, $i = 1,2$):

1. For $n_1 > 0$ and $n_2 > 0$ and setting $\theta_{F_i n_i} = \operatorname{argmin} F_i n_i(\cdot)$,

$$\hat{F}_i(\alpha,\beta,n_i) = F_i n_i(\alpha \vee \theta_{F_i n_i}) \vee F_i n_i(\beta \wedge \theta_{F_i n_i}), \quad i = 1,2. \tag{3.33}$$

2. For $n_1 < 0$ and $n_2 > 0$ and $\theta_{F_1 n_1} = \operatorname{argmax} F_1 n_1(\cdot)$ and $\theta_{F_2 n_2} = \operatorname{argmin} F_2 n_2(\cdot)$,

$$\begin{aligned} \hat{F}_1(\alpha, \beta, n_1) &= F_1 n_1(\alpha \wedge \theta_{F_1 n_1}) \wedge F_1 n_1(\beta \vee \theta_{F_1 n_1}), \\ \hat{F}_2(\alpha, \beta, n_2) &= F_2 n_2(\alpha \vee \theta_{F_2 n_2}) \vee F_2 n_2(\beta \wedge \theta_{F_2 n_2}). \end{aligned} \tag{3.34}$$

3. For $n_1 > 0$ and $n_2 < 0$ and setting $\theta_{F_1 n_1} = \operatorname{argmin} F_1 n_1(\cdot)$ and $\theta_{F_2 n_2} = \operatorname{argmax} F_2 n_2(\cdot)$,

$$\begin{aligned} \hat{F}_1(\alpha, \beta, n_1) &= F_1 n_1(\alpha \vee \theta_{F_1 n_1}) \vee F_1 n_1(\beta \wedge \theta_{F_1 n_1}), \\ \hat{F}_2(\alpha, \beta, n_2) &= F_2 n_2(\alpha \wedge \theta_{F_2 n_2}) \wedge F_2 n_2(\beta \vee \theta_{F_2 n_2}). \end{aligned} \tag{3.35}$$

4. For $n_1 < \tilde{h}0$ and $n_2 < 0$ and setting $\theta_{F_i n_i} = \operatorname{argmax} F_i n_i(\cdot)$,

$$\hat{F}_i(\alpha, \beta, n_i) = F_i n_i(\alpha \wedge \theta_{F_i n_i}) \wedge F_i n_i(\beta \vee \theta_{F_i n_i}), \quad i = 1, 2. \tag{3.36}$$

Lemma 4 *The numerical flux $\tilde{h}$ defined by (3.32)–(3.36) satisfies the following essential properties.*

(i) It is consistent, that is, $\tilde{h}(\phi, \phi, \boldsymbol{n}) = \mathbf{F}(\phi) \cdot \boldsymbol{n}$ for all ϕ.
(ii) It is monotone, that is, for given $\boldsymbol{n}$, $\tilde{h}(\alpha, \beta, \boldsymbol{n})$ is a non-decreasing function of α and a non-increasing function of β.
(iii) It is conservative, i.e., $\tilde{h}(\alpha, \beta, \boldsymbol{n}) = -\tilde{h}(\beta, \alpha, -\boldsymbol{n})$.

Proof. For the consistency, let us concentrate on the case $n_1 > 0$ and $n_2 < 0$. It holds that

$$\begin{aligned} &\tilde{h}(\beta, \alpha, -\boldsymbol{n}) \\ &= \hat{F}_1(\beta, \alpha, -n_1) + \hat{F}_2(\beta, \alpha, -n_2) \\ &= \big(-F_1 n_1(\beta \wedge \theta_{-F_1 n_1}) \wedge -F_1 n_1(\alpha \vee \theta_{-F_1 n_1})\big) + \big(-F_2 n_2(\beta \vee \theta_{-F_2 n_2}) \vee -F_2 n_2(\alpha \wedge \theta_{-F_2 n_2})\big) \\ &= -\big(F_1 n_1(\beta \wedge \theta_{-F_1 n_1}) \vee F_1 n_1(\alpha \vee \theta_{-F_1 n_1})\big) - \big(F_2 n_2(\beta \vee \theta_{-F_2 n_2}) \wedge F_2 n_2(\alpha \wedge \theta_{-F_2 n_2})\big) \\ &= -\big(F_1 n_1(\alpha \vee \theta_{-F_1 n_1}) \vee F_1 n_1(\beta \wedge \theta_{-F_1 n_1})\big) - \big(F_2 n_2(\alpha \wedge \theta_{-F_2 n_2}) \wedge F_2 n_2(\beta \vee \theta_{-F_2 n_2})\big) \\ &= -\hat{F}_1(\alpha, \beta, n_1) - \hat{F}_2(\alpha, \beta, n_2) = -\tilde{h}(\alpha, \beta, \boldsymbol{n}). \end{aligned}$$

The remaining properties can be readily established. ∎

Since the flux vector $\mathbf{F}$ as given by (1.2) is in general discontinuous in $\boldsymbol{x}$, we apply the modified Godunov flux reconstruction proposed in [1]. The DFLU numerical flux is defined as

$$h(\alpha, \beta, \boldsymbol{u}_h(\boldsymbol{x}), \boldsymbol{x}, \boldsymbol{n}) = \hat{F}_1(\alpha, \beta, n_1) + \hat{F}_2(\alpha, \beta, n_2), \tag{3.37}$$

where the numerical flux components $\hat{F}_1$ and $\hat{F}_2$ are now computed by considering the following cases, where we use the notation $F_i^- n_i(\cdot) = F_i(\cdot, \boldsymbol{u}_h(\boldsymbol{x}), \boldsymbol{x}^-) n_i$ and $F_i^+ n_i(\cdot) = F_i(\cdot, \boldsymbol{u}_h(\boldsymbol{x}), \boldsymbol{x}^+) n_i)$. Since these components $F_i^- n_i$ and $F_i^+ n_i$ follow the hypothesis (H_1) and (H_2) of [1], the corresponding expression for the numerical fluxes can be listed as follows:

1. For $n_1 > 0$ and $n_2 > 0$, and setting $\theta_{F_i^- n_i} = \operatorname{argmin} F_i^- n_i(\cdot)$,

$$\hat{F}_i(\alpha, \beta, n_i) = F_i^- n_i\big(\alpha \vee \theta_{F_i^- n_i}\big) \vee F_i^+ n_i\big(\beta \wedge \theta_{F_i^+ n_i}\big), \quad i = 1, 2. \tag{3.38}$$

2. For $n_1 < 0$ and $n_2 > 0$ and setting $\theta_{F_1^- n_1} = \operatorname{argmax} F_1^- n_1(\cdot)$ and $\theta_{F_2^- n_2} = \operatorname{argmin} F_2^- n_2(\cdot)$,

$$\begin{aligned} \hat{F}_1(\alpha, \beta, n_1) &= F_1^- n_1\big(\alpha \wedge \theta_{F_1^- n_1}\big) \wedge F_1^+ n_1\big(\beta \vee \theta_{F_1^+ n_1}\big), \\ \hat{F}_2(\alpha, \beta, n_2) &= F_2^- n_2\big(\alpha \vee \theta_{F_2^- n_2}\big) \vee F_2^+ n_2\big(\beta \wedge \theta_{F_2^+ n_2}\big). \end{aligned} \tag{3.39}$$

3. For $n_1 > 0$ and $n_2 < 0$ and setting $\theta_{F_1^- n_1} = \operatorname{argmin} F_1^- n_1(\cdot)$ and $\theta_{F_2^- n_2} = \operatorname{argmax} F_2^- n_2(\cdot)$,

$$\begin{aligned} \hat{F}_1(\alpha, \beta, n_1) &= F_1^- n_1\big(\alpha \vee \theta_{F_1^- n_1}\big) \vee F_1^+ n_1\big(\beta \wedge \theta_{F_1^+ n_1}\big), \\ \hat{F}_2(\alpha, \beta, n_2) &= F_2^- n_2\big(\alpha \wedge \theta_{F_2^- n_2}\big) \wedge F_2^+ n_2\big(\beta \vee \theta_{F_2^+ n_2}\big). \end{aligned} \tag{3.40}$$

4. For $n_1 < 0$, $n_2 < 0$ and $\theta_{F_i^- n_i} = \operatorname{argmax} F_i^- n_i(\cdot)$,

$$\hat{F}_i(\alpha, \beta, n_i) = F_i^- n_i\big(\alpha \wedge \theta_{F_i^- n_i}\big) \wedge F_i^+ n_i\big(\beta \vee \theta_{F_i^+ n_i}\big), \quad i = 1, 2. \tag{3.41}$$

Corollary 1 *For fixed values of $\boldsymbol{u}_h(\boldsymbol{x})$, $\boldsymbol{x}$ and $\boldsymbol{n}$, the numerical flux h defined by (3.37)–(3.41) satisfies the following essential properties.*

(i) It is monotone, that is, for given $\boldsymbol{n}$, $h(\alpha, \beta, \boldsymbol{u}_h(\boldsymbol{x}), \boldsymbol{x}, \boldsymbol{n})$ is a non-decreasing function of α and a non-increasing function of β.
(ii) It is conservative, i.e., $h(\alpha, \beta, \boldsymbol{u}_h(\boldsymbol{x}), \boldsymbol{x}, \boldsymbol{n}) = -h(\beta, \alpha, \boldsymbol{u}_h(\boldsymbol{x}), \boldsymbol{x}, -\boldsymbol{n})$.

Note that the flux h defined by (3.37)–(3.41) is discontinuous in the spatial variable, and therefore the numerical flux is, in general, *not* consistent.

3.5 Fully discrete DG formulation

We now choose a basis $\{\psi_1, \dots \psi_L\}$ for the space S_h^k and write the approximation of a given function ϕ_h in such a space as

$$\phi_h(\boldsymbol{x}, t) \approx \sum_{j=1}^{L} \phi_j^K(t) \psi_j(\boldsymbol{x}). \tag{3.42}$$

Replacing ϕ_h in (3.31) by the right-hand side of (3.42) yields

$$\begin{aligned} &\frac{\mathrm{d}}{\mathrm{d}t} \sum_{j=1}^{L} \phi_j^K(t)(\psi_j, s_h)_K - \sum_{j=1}^{M} \bar{\omega}_j \mathbf{F}\big(\phi_h(\boldsymbol{x}_{K_j}, t), \boldsymbol{u}_h(\boldsymbol{x}_{K_j})\big) \cdot \nabla s_h(\boldsymbol{x}_{K_j}) |K| \\ &+ \sum_{e \in \partial K} \sum_{i=1}^{N} \omega_i h\big(\phi_h(\boldsymbol{x}_{i,e}^{\mathrm{int}(K)}, t), \phi_h(\boldsymbol{x}_{i,e}^{\mathrm{ext}(K)}, t), \boldsymbol{u}_h^e, \boldsymbol{x}_{i,e}, \boldsymbol{n}_e\big) s_h(\boldsymbol{x}_{i,e}) |e| = 0 \quad \forall s_h \in S_h^k. \end{aligned} \tag{3.43}$$

After defining $\boldsymbol{\phi}_h^K(t) := (\phi_1^K(t), \dots, \phi_L^K(t))^{\mathrm{T}}$ and choosing $s_h = \psi_k$ for $k = 1, \dots, L$ in (3.43), we can assert that

$$\frac{\mathrm{d}}{\mathrm{d}t} \boldsymbol{\phi}_h^K(t) = -\mathbf{A}^{-1}(\boldsymbol{b} + \boldsymbol{c}), \tag{3.44}$$

where $\mathbf{A} = (a_{jk})_{L \times L}$, $\boldsymbol{b} = (b_1, \dots, b_L)^{\mathrm{T}}$, and $\boldsymbol{c} = (c_1, \dots, c_L)^{\mathrm{T}}$ with

$$a_{jk} = \big(\psi_j(\boldsymbol{x}), \psi_k(\boldsymbol{x})\big)_K, \quad b_k = -\sum_{j=1}^{M} \bar{\omega}_j \mathbf{F}\big(\phi_h(\boldsymbol{x}_{K_j}, t), \boldsymbol{u}_h(\boldsymbol{x}_{K_j})\big) \cdot \nabla \psi_k(\boldsymbol{x}_{K_j}) |K|,$$

$$c_k = \sum_{e \in \partial K} \sum_{i=1}^{N} \omega_i h\big(\phi_h(\boldsymbol{x}_{i,e}^{\mathrm{int}(K)}, t), \phi_h(\boldsymbol{x}_{i,e}^{\mathrm{ext}(K)}, t), \boldsymbol{u}_h^e, \boldsymbol{x}_{i,e}, \boldsymbol{n}_e\big) \psi_k(\boldsymbol{x}_{e,i}) |e|, \quad j, k = 1, \dots, L.$$

Next we apply a forward Euler discretization in the time variable from t^n to t^{n+1}, which yields

$$\boldsymbol{\phi}_h^K(t^{n+1}) = \boldsymbol{\phi}_h^K(t^n) - \Delta t \mathbf{A}^{-1}(\boldsymbol{b} + \boldsymbol{c}),$$

and therefore the local approximation for ϕ is computed from

$$\phi_h(\boldsymbol{x}, t^{n+1}) = \big(\psi_1(\boldsymbol{x}), \dots, \psi_L(\boldsymbol{x})\big) \boldsymbol{\phi}_h^K(t^{n+1}) \quad \forall \boldsymbol{x} \in K.$$

Now, introducing the right hand side operator L_h, we may recast (3.44) as

$$\frac{\mathrm{d}}{\mathrm{d}t} \boldsymbol{\phi}_h^K(t) = L_h\big(\boldsymbol{\phi}_h^K(t)\big).$$

3.6 Limiter for triangular elements

Plain high-order DG formulations ($k \geq 1$) typically lack general stability properties exhibited by low-order methods, and therefore one should expect that spurious oscillations develop. However, this issue can be resolved, for instance, by applying a limiter to the new solution at time t^{n+1}:

$$\phi_h^{n+1} = \Lambda\Pi_h\big(\phi_h(\boldsymbol{x}, t^{n+1})\big),$$

where the limiting operator $\Lambda\Pi_h$ (i) should not change the cell average value, and (ii) it should not affect the accuracy of the overall scheme in smooth regions. The RKDG method with limiters follows the steps outlined in Algorithm 1.

Algorithm 1 Runge-Kutta discontinuous Galerkin method with limiters.

compute **and** store the mass matrix
determine ϕ_h^0 by an L^2-projection of the initial condition ϕ_0
apply the slope limiter to ϕ_h^0 **and** recover the new value $\phi_h^0 = \Lambda\Pi_h(\phi_h^0)$
for $n = 0, 1, \ldots$ **do**
    compute the time step from the CFL condition
    set initial datum $\phi_h^{n,0} = \phi_h^n$
    perform RK stages:
    for $r = 0, 1, \ldots, N_{rk} - 1$ **do**
        compute right hand side $L_h(\phi_h^{n,r})$
        update solution to employ in the next RK stage

$$\phi_h^{n,r} \to \phi_h^{n,r+1}$$

        apply limiter

$$\phi_h^{n,r+1} = \Lambda\Pi_h \phi_h^{n,r+1}$$

    end for
end for

For triangular finite elements, we follow the method in [17] to define the limiting operator $\Lambda\Pi_h$. For a piecewise linear function ϕ_h, the limiter possesses the following properties.

1. Accuracy: if ϕ_h is a linear function, then $\Lambda\Pi_h\phi_h = \phi_h$.
2. Conservation of mass: for every element K of the triangulation $\mathcal{T}_h$, we have

$$\int_K \Lambda\Pi_h\phi_h \,\mathrm{d}\boldsymbol{x} = \int_K \phi_h \,\mathrm{d}\boldsymbol{x}.$$

3. Slope limiting: on each element K of $\mathcal{T}_h$ the gradient of $\Lambda\Pi_h\phi_h$ is not larger than that of ϕ_h.

Let us consider the triangulation in Figure 1, where b_i denotes the barycenter of the corresponding triangle K_i for $i = 0, 1, 2, 3$ and m_1 is the midpoint of the edge joining the triangle K_0 and K_1. For some $\alpha_1, \alpha_2 \geq 0$, we can write $m_1 - b_0 = \alpha_2(b_1 - b_0) + \alpha_2(b_2 - b_0)$.

For any linear function ϕ_h we have the following identities:

$$\phi_h(m_1) - \phi_h(b_0) = \alpha_1\big(\phi_h(b_1) - \phi_h(b_0)\big) + \alpha_2\big(\phi_h(b_1) - \phi_h(b_0)\big)$$

and

$$\bar{\phi}_{K_i} = \frac{1}{K_i}\int_{K_i} \phi_h \,\mathrm{d}\boldsymbol{x} = \phi_h(b_i), \quad i = 0, 1, 2, 3.$$

Thus, we can write

$$\tilde{\phi}_h(m_1, K_0) \equiv \phi_h(m_1) - \bar{\phi}_{K_0} = \alpha_1(\bar{\phi}_{K_1} - \bar{\phi}_{K_0}) + \alpha_2(\bar{\phi}_{K_2} - \bar{\phi}_{K_0}) \equiv\triangle\ \bar{\phi}(m_1, K_0).$$

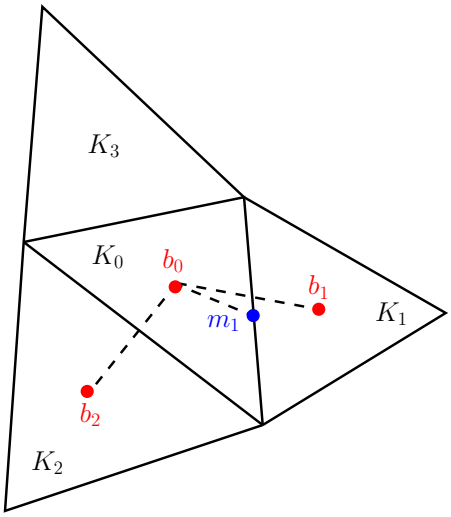

Fig. 1 Sketch of the mesh entities employed in the limiting procedure.

Now if we choose a nodal Lagrangian basis $\{\psi_1, \psi_2, \psi_3\}$ for each element K such that each basis function takes the value one at one of the midpoints and zero at the remaining midpoints, then for any $\boldsymbol{x} \in K_0$ we can write

$$\phi_h(\boldsymbol{x}) = \sum_{i=1}^{3} \phi_h(m_i)\psi_i(\boldsymbol{x}) = \bar{\phi}_{K_0} + \sum_{i=1}^{3} \tilde{\phi}_h(m_i, K_0)\psi_i(\boldsymbol{x}),$$

where m_1, m_2, m_3 are the midpoints of the triangle K_0. To compute $\mathit{\Lambda\Pi}_h$, we first obtain the quantities

$$\triangle_i = \bar{m}\big\{\tilde{\phi}_h(m_i, K_0), \nu \triangle \bar{\phi}(m_i, K_0))\big\},$$

where $\nu > 1$ and $\bar{m}$ is the modified min-mod function defined as follows:

$$\bar{m}(a_1, a_2, \cdots, a_m) = \begin{cases} a_1 & \text{if } |a_1| \leq Mh^2, \\ \text{minmod}(a_1, a_2, \cdots, a_m) & \text{otherwise,} \end{cases}$$

with the min-mod function is defined by

$$\text{minmod}(a_1, a_2, \cdots, a_m) = \begin{cases} s \min\{|a_1|, \ldots, |a_m|\} & \text{if } s = \text{sgn}(a_1) = \text{sgn}(a_2) = \cdots = \text{sgn}(a_m), \\ 0 & \text{otherwise,} \end{cases}$$

where M is an upper bound on the absolute value of the second derivative of ϕ_h and h is the diameter of the cell K_0. Then, if $\sum_{i=1}^{3} \triangle_i = 0$, we simply set

$$\phi_h(\boldsymbol{x}) = \bar{\phi}_{K_0} + \sum_{i=1}^{3} \triangle_i \, \psi_i(\boldsymbol{x}).$$

If $\sum_{i=1}^{3} \triangle_i \neq 0$ we compute

$$\sigma^+ = \sum_{i=1}^{3} 0 \vee \triangle_i, \quad \sigma^- = \sum_{i=1}^{3} 0 \vee - \triangle_i$$

and set $\theta^+ = \min\{1, \sigma^-/\sigma^+\}$, $\theta^- := \min\{1, \sigma^+/\sigma^-\}$. Then we define

$$\phi_h(\boldsymbol{x}) = \bar{\phi}_{K_0} + \sum_{i=1}^{3} \hat{\triangle}_i \psi_i(\boldsymbol{x}), \quad \text{where } \hat{\triangle}_i = \theta^+(0 \vee \triangle_i) - \theta^-(0 \vee - \triangle_i).$$

4 Stability analysis for saturation

Let us assume that the velocity $\boldsymbol{u}_h$ has been computed previously. If we choose $s_h(\boldsymbol{x}) \equiv 1$ in S_h^K, then equation (3.29) takes the form

$$\frac{\mathrm{d}}{\mathrm{d}t}\int_K \phi_h(\boldsymbol{x},t)\,\mathrm{d}\boldsymbol{x} + \sum_{e\in\partial K}\int_e \mathbf{F}(\phi_h(\boldsymbol{x},t),\boldsymbol{u}_h,\boldsymbol{x})\cdot\boldsymbol{n}_{e,K}\,\mathrm{d}s = 0.$$

We denote

$$\bar{\phi}_K(t) := \frac{1}{|K|}\int_K \phi_h(\boldsymbol{x},t)\,\mathrm{d}\boldsymbol{x}, \quad \bar{\phi}_K^n := \bar{\phi}_K(t^n).$$

After adopting a forward Euler time stepping we end up with the equation

$$\bar{\phi}_K^{n+1} = \bar{\phi}_K^n - \frac{\Delta t}{|K|}\sum_{i=1}^{3}\int_{e_K^i}\mathbf{F}(\phi_K,\boldsymbol{u}_h,\boldsymbol{x})\cdot\boldsymbol{n}^i\,\mathrm{d}s, \tag{4.1}$$

where we have enumerated the edges of the triangle K by $e_K^i, i = 1,2,3$, and $\boldsymbol{n}_i$ are the corresponding normal vector to each edge e_K^i. Here the solution $\bar{\phi}_K^n$ is the average of the DG polynomial computed at the time step t^n, say

$$\bar{\phi}_K^n = \frac{1}{|K|}\int_K p_K(\boldsymbol{x})\,\mathrm{d}\boldsymbol{x},$$

where $p_K(\boldsymbol{x})$ is the corresponding DG polynomial of degree k in each of its variable. In this section we verify that the DG approximated saturation profile satisfies a maximum principle in the mean $\bar{\phi}_K^n$. In order to prove this property we modify the method adopted in [37] to the case of discontinuous flux function.

The term $\mathbf{F}\big(\phi_h(\boldsymbol{x},t),\boldsymbol{u}_h(\boldsymbol{x}),x\big)\cdot\boldsymbol{n}^i$ in the integral is approximated by the numerical flux as

$$\mathbf{F}\big(\phi_h(\boldsymbol{x},t),\boldsymbol{u}_h(\boldsymbol{x}),x\big)\cdot\boldsymbol{n}^i \approx h\big(\phi_h(\boldsymbol{x}^{\mathrm{int}(K)},t),\phi_h(\boldsymbol{x}^{\mathrm{ext}(K)},t),\boldsymbol{u}_h(\boldsymbol{x}),\boldsymbol{x},\boldsymbol{n}^i\big).$$

Inserting this into equation (4.1) yields

$$\bar{\phi}_K^{n+1} = \bar{\phi}_K^n - \frac{\Delta t}{|K|}\sum_{i=1}^{3}\int_{e_K^i} h\big(\phi_h(\boldsymbol{x}^{\mathrm{int}(K)},t),\phi_h(\boldsymbol{x}^{\mathrm{ext}(K)},t),\boldsymbol{u}_h(\boldsymbol{x}),\boldsymbol{x},\boldsymbol{n}^i\big)\,\mathrm{d}s. \tag{4.2}$$

Since the approximated DG polynomial $p_K(\boldsymbol{x})$ is of degree k in each variable, we need to approximate the edge integral in (4.2) by the $(k+1)$-point Gauss quadrature rule. Let $\{\boldsymbol{x}_\beta^i, \beta = 1,\dots,k+1\}$ denote the set of quadrature points corresponding to the edges $e_K^i, i = 1,2,3$. Also we use the following notation:

$$\phi_{i,\beta}^{\mathrm{int}(K)} = \phi_h\big(\boldsymbol{x}_\beta^{i\ \mathrm{int}(K)}\big), \quad \phi_{i,\beta}^{\mathrm{ext}(K)} = \phi_h\big(\boldsymbol{x}_\beta^{i\ \mathrm{ext}(K)}\big), \quad \boldsymbol{u}_\beta^i = \boldsymbol{u}_h\big(\boldsymbol{x}_\beta^i\big).$$

Thus, the formulation (4.2) reduces to

$$\bar{\phi}_K^{n+1} = \bar{\phi}_K^n - \frac{\Delta t}{|K|}\sum_{i=1}^{3}\sum_{\beta=1}^{k+1} h\big(\phi_{i,\beta}^{\mathrm{int}(K)},\phi_{i,\beta}^{\mathrm{ext}(K)},\boldsymbol{u}_\beta^i,\boldsymbol{x}_\beta^i,\boldsymbol{n}^i\big)\omega_\beta|e_K^i|,$$

where $|e_K^i|$ denotes the measure of edges of the triangle K and $\omega_1,\dots,\omega_{k+1}$ denote the $k+1$ weights of the Gauss quadrature rule in the interval $[-\frac{1}{2},\frac{1}{2}]$, which have the property $\omega_1+\cdots+\omega_{k+1} = 1$.

Now we split $\bar{\phi}_K^n$ into point values of the DG polynomial $p_K(\boldsymbol{x})$ using a quadrature rule on the rectangle $[-\frac{1}{2},\frac{1}{2}]$. For simplicity in the expression we denote by $\mathbf{V}_1,\mathbf{V}_2$ and $\mathbf{V}_3$ the three vertices of the triangle K which is chosen in a clock wise order. We can represent the position vector P of any point in the triangle K in terms of barycentric coordinates as $P = \zeta_1\mathbf{V}_1+\zeta_2\mathbf{V}_2+\zeta_3\mathbf{V}_3$. In the

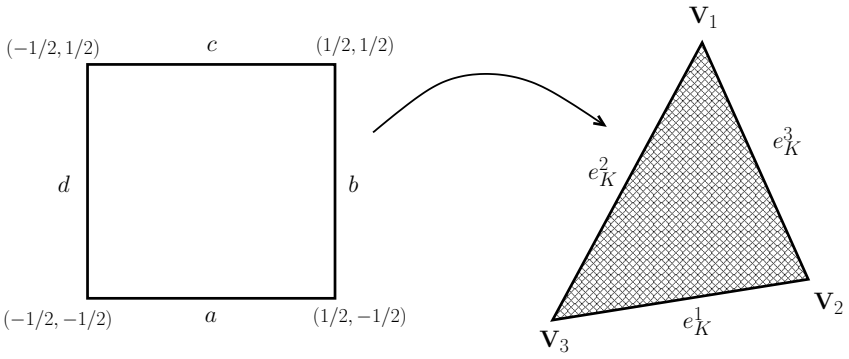

Fig. 2 Representation of the projection map between the rectangular and triangular reference elements.

first step the rectangle $[-\frac{1}{2},\frac{1}{2}]\times[-\frac{1}{2},\frac{1}{2}]$ taken in the (u,v) plane is mapped on to the triangle by a set of functions, which are

$$\begin{aligned}
\boldsymbol{\varphi}_1(u,v) &= \left(\frac{1}{2}+v\right)\mathbf{V}_1 + \left(\frac{1}{2}+u\right)\left(\frac{1}{2}-v\right)\mathbf{V}_2 + \left(\frac{1}{2}-u\right)\left(\frac{1}{2}-v\right)\mathbf{V}_3,\\
\boldsymbol{\varphi}_2(u,v) &= \left(\frac{1}{2}-u\right)\left(\frac{1}{2}-v\right)\mathbf{V}_1 + \left(\frac{1}{2}+v\right)\mathbf{V}_2 + \left(\frac{1}{2}+u\right)\left(\frac{1}{2}-v\right)\mathbf{V}_3,\\
\boldsymbol{\varphi}_3(u,v) &= \left(\frac{1}{2}+u\right)\left(\frac{1}{2}-v\right)\mathbf{V}_1 + \left(\frac{1}{2}-u\right)\left(\frac{1}{2}-v\right)\mathbf{V}_2 + \left(\frac{1}{2}+v\right)\mathbf{V}_3.
\end{aligned}$$

Each of the functions maps one of the sides of the rectangle onto one vertex of K and the other sides of the rectangles to edges of the triangle K. Now we can write

$$\bar{\phi}_K^n = \frac{1}{|K|}\int_K p_K(\boldsymbol{x})\,\mathrm{d}\boldsymbol{x} = \frac{1}{|K|}\int_{-1/2}^{1/2}\int_{-1/2}^{1/2} p_K(\boldsymbol{\varphi}_i(u,v))\left|\frac{\partial\boldsymbol{\varphi}_i(u,v)}{\partial(u,v)}\right|\mathrm{d}u\,\mathrm{d}v \quad \text{for } i=1,2,3, \tag{4.3}$$

where the determinant of the Jacobian $\partial\boldsymbol{\varphi}_i(u,v)/\partial(u,v)$ can be easily computed as

$$\left|\frac{\partial\boldsymbol{\varphi}_i(u,v)}{\partial(u,v)}\right| = 2|K|\left(\frac{1}{2}-v\right).$$

Let $\{v_\beta,\beta=1,\ldots,k+1\}$ denote $k+1$ Gauss quadrature points chosen on the interval $[-\frac{1}{2},\frac{1}{2}]$ with the corresponding quadrature weights ω_β. Also let $\{u_\alpha,\alpha=1,\ldots,N\}$ denote N Gauss-Lobatto quadrature points chosen on the interval $[-\frac{1}{2},\frac{1}{2}]$ with corresponding weight $\hat{\omega}_\alpha$, and where N is the smallest integer such that $2N-3\geq k$. The tensor product of these two types of quadrature points are used to define the quadrature rule on the rectangle $[-\frac{1}{2},\frac{1}{2}]\times[-\frac{1}{2},\frac{1}{2}]$. Therefore the quadrature points could be taken as $S_K=\{(u_\alpha,v_\beta),\alpha=1,\ldots,N,\beta=1,\ldots,k+1\}$, which yields exact quadrature for a polynomial $p(u,v)$ of degree less or equal k in u, and of degree less or equal $2k+1$ in v.

We now define the following polynomial of degree k and $k+1$ in u and v, respectively:

$$\hat{p}_K^i(u,v) = p_K\big(\boldsymbol{\varphi}_i(u,v)\big)\left|\frac{\partial\boldsymbol{\varphi}_i(u,v)}{\partial(u,v)}\right| = 2|K|p_K\big(\boldsymbol{\varphi}_i(u,v)\big)\left(\frac{1}{2}-v\right).$$

Then (4.3) can be written as

$$\bar{\phi}_K^n = \frac{1}{|K|}\sum_{\alpha=1}^{N}\sum_{\beta=1}^{k+1}\hat{p}_K^i(u_\alpha,v_\beta)\hat{\omega}_\alpha\omega_\beta = 2\sum_{\alpha=1}^{N}\sum_{\beta=1}^{k+1}p_K\big(\boldsymbol{\varphi}_i(u_\alpha,v_\beta)\big)\left(\frac{1}{2}-v_\beta\right)\hat{\omega}_\alpha\omega_\beta. \tag{4.4}$$

Now for each $i=1,2,3$ the set of points $\{\boldsymbol{\varphi}_i(S_K)\}$ acts as the set of quadrature points for the polynomial $p_K(\boldsymbol{x})$. Combination of these sets of quadrature points leads to a total of $3(N-1)(k+1)$

quadrature points, which we denote by $\hat{S}_K = \{\boldsymbol{\varphi}_1(S_K)\} \cup \{\boldsymbol{\varphi}_2(S_K)\} \cup \{\boldsymbol{\varphi}_3(S_K)\}$. In this way, the cell average in (4.4) takes the form

$$\begin{aligned}\bar{\phi}_K^n &= \frac{1}{3}\sum_{i=1}^{3} \bar{\phi}_K^n = \frac{1}{3|K|}\sum_{i=1}^{3}\sum_{\alpha=1}^{N}\sum_{\beta=1}^{k+1} \hat{p}_K^i(u_\alpha, v_\beta)\hat{\omega}_\alpha\omega_\beta \\ &= \sum_{i=1}^{3}\sum_{\alpha=1}^{N}\sum_{\beta=1}^{k+1} p_K(\boldsymbol{\varphi}_i(u_\alpha, v_\beta))\frac{2}{3}\left(\frac{1}{2} - v_\beta\right)\hat{\omega}_\alpha\omega_\beta = \sum_{\boldsymbol{x}\in\hat{S}_K} p_K(\boldsymbol{x})\omega_x.\end{aligned} \tag{4.5}$$

Consider now the quadrature points on the edges e_K^i of K. Note that $\boldsymbol{\varphi}_1(a)$, $\boldsymbol{\varphi}_2(b)$ and $\boldsymbol{\varphi}_3(d)$ are mapped onto the edge e_K^1 (see the sketch in Figure 2), but the side a does not contain any quadrature points, and therefore the quadrature points on e_K^1 are only $\boldsymbol{\varphi}_2(\frac{1}{2}, v_\beta) \cup \boldsymbol{\varphi}_3(-\frac{1}{2}, v_\beta)$. This implies that the quadrature points on e_K^1 can be written in terms of barycentric coordinates as $(0, \frac{1}{2} + v_\beta, \frac{1}{2} - v_\beta)$ (which are the quadrature points $\{\boldsymbol{\varphi}_3(-\frac{1}{2}, v_\beta)\} = \{\boldsymbol{\varphi}_3(-\frac{1}{2}, -v_\beta)\} = \{\boldsymbol{\varphi}_2(\frac{1}{2}, v_\beta)\}$). In a similar manner, the quadrature points associated to e_K^2 are $(\frac{1}{2} - v_\beta, 0, \frac{1}{2} + v_\beta)$, and those on the edge e_K^3 are $(\frac{1}{2} + v_\beta, \frac{1}{2} - v_\beta, 0)$.

The weight of the point $(0, \frac{1}{2} + v_\beta, \frac{1}{2} - v_\beta)$ is calculated as $\hat{\omega}_1 = \hat{\omega}_N$, and thus

$$\frac{1}{2}\left(\frac{1}{2} + v_\beta\right)\omega_\beta\hat{\omega}_1 + \frac{2}{3}\left(\frac{1}{2} - v_\beta\right)\omega_\beta\hat{\omega}_N = \frac{2}{3}\omega_\beta\hat{\omega}_1.$$

Similarly, the weights on the edges e_K^2 and e_K^3 are computed as $\frac{2}{3}\omega_\beta\hat{\omega}_1$.

Let us denote by $\phi_{i,\beta}^{\mathrm{int}(K)}$ and ϕ_ν^{int} the values of the polynomial at the quadrature points on the edges and interior of the triangle K respectively. Also the quadrature weights corresponds to the values ϕ_ν^{int} is denoted by $\tilde{\omega}_\nu$. We have $M = 3(N-2)(k+1)$ quadrature points in the interior of the triangle. Now the expression (4.5) becomes

$$\bar{\phi}_K^n = \sum_{i=1}^{3}\sum_{\beta=1}^{k+1} \phi_{i,\beta}^{\mathrm{int}(K)}\frac{2}{3}\omega_\beta\hat{\omega}_1 + \sum_{\nu=1}^{M}\phi_\nu^{\mathrm{int}}\tilde{\omega}_\nu, \tag{4.6}$$

and we write the value of $\bar{\phi}_K^{n+1}$ as

$$\bar{\phi}_K^{n+1} = H\big(\phi_{1,1}^{\mathrm{int}(K)}, \phi_{1,2}^{\mathrm{int}(K)}, \ldots, \phi_{3,k+1}^{\mathrm{int}(K)}, \phi_{1,1}^{\mathrm{ext}(K)}, \phi_{1,2}^{\mathrm{ext}(K)}, \ldots, \phi_{3,k+1}^{\mathrm{ext}(K)}, \phi_1^{\mathrm{int}}, \ldots, \phi_M^{\mathrm{int}}\big). \tag{4.7}$$

For ease of reference, we denote the right-hand side of (4.7) by $H(\ldots)$.

Lemma 5 *The function H in (4.7) is increasing in each of its variable provided the following CFL condition is satisfied*

$$\frac{\Delta t}{|K|}\sum_{i=1}^{3}|e_K^i| \le \frac{2}{3}\hat{\omega}_1, \tag{4.8}$$

where $\hat{\omega}_1$ is the first weight of the Gauss-Lobatto quadrature rule on $[-\frac{1}{2}, \frac{1}{2}]$.

Proof. We have

$$H(\ldots) = \bar{\phi}_K^n - \frac{\Delta t}{|K|}\sum_{\beta=1}^{k+1}\omega_\beta\sum_{i=1}^{3} h\big(\phi_{i,\beta}^{\mathrm{int}(K)}, \phi_{i,\beta}^{\mathrm{ext}(K)}, \boldsymbol{u}_\beta^i, \boldsymbol{x}_\beta^i, \boldsymbol{n}^i\big)|e_K^i|.$$

Using the conservativity of the numerical flux, we can assert that

$$\begin{aligned}&\sum_{i=1}^{3} h\big(\phi_{i,\beta}^{\mathrm{int}(K)}, \phi_{i,\beta}^{\mathrm{ext}(K)}, \boldsymbol{u}_\beta^i, \boldsymbol{x}_\beta^i, \boldsymbol{n}^i\big)|e_K^i| \\ &= h\big(\phi_{1,\beta}^{\mathrm{int}(K)}, \phi_{1,\beta}^{\mathrm{ext}(K)}, \boldsymbol{u}_\beta^1, \boldsymbol{x}_\beta^1, \boldsymbol{n}^1\big)|e_K^1| + h\big(\phi_{1,\beta}^{\mathrm{int}(K)}, \phi_{2,\beta}^{\mathrm{int}(K)}, \boldsymbol{u}_\beta^1, \boldsymbol{x}_\beta^1, -\boldsymbol{n}^1\big)|e_K^1| \\ &\quad + h\big(\phi_{2,\beta}^{\mathrm{int}(K)}, \phi_{1,\beta}^{\mathrm{int}(K)}, \boldsymbol{u}_\beta^1, \boldsymbol{x}_\beta^1, \boldsymbol{n}^1\big)|e_K^1| + h\big(\phi_{2,\beta}^{\mathrm{int}(K)}, \phi_{2,\beta}^{\mathrm{ext}(K)}, \boldsymbol{u}_\beta^2, \boldsymbol{x}_\beta^2, \boldsymbol{n}^2\big)|e_K^2|\end{aligned}$$

$$+ h\big(\phi_{2,\beta}^{\mathrm{int}(K)}, \phi_{3,\beta}^{\mathrm{int}(K)}, \boldsymbol{u}_\beta^3, \boldsymbol{x}_\beta^3, \boldsymbol{n}^3\big)|e_K^3| + h\big(\phi_{3,\beta}^{\mathrm{int}(K)}, \phi_{2,\beta}^{\mathrm{int}(K)}, \boldsymbol{u}_\beta^3, \boldsymbol{x}_\beta^3, -\boldsymbol{n}^3\big)|e_K^3|$$
$$+ h\big(\phi_{3,\beta}^{\mathrm{int}(K)}, \phi_{3,\beta}^{\mathrm{ext}(K)}, \boldsymbol{u}_\beta^3, \boldsymbol{x}_\beta^3, \boldsymbol{n}^3\big)|e_K^3|.$$

On the other hand, we have

$$\begin{aligned} H(\dots) &= \sum_{i=1}^{3}\sum_{\beta=1}^{k+1} \phi_{i,\beta}^{\mathrm{int}(K)} \frac{2}{3}\omega_\beta\hat{\omega}_1 + \sum_{\nu=1}^{M} \phi_\nu^{\mathrm{int}}\tilde{\omega}_\nu - \frac{\Delta t}{|K|}\sum_{\beta=1}^{k+1}\omega_\beta \sum_{i=1}^{3} h\big(\phi_{i,\beta}^{\mathrm{int}(K)}, \phi_{i,\beta}^{\mathrm{ext}(K)}, \boldsymbol{u}_\beta^i, \boldsymbol{x}_\beta^i, \boldsymbol{n}^i\big)|e_K^i| \\ &= \sum_{\nu=1}^{M} \phi_\nu^{\mathrm{int}}\tilde{\omega}_\nu + \sum_{\beta=1}^{k+1}\frac{2}{3}\omega_\beta\hat{\omega}_1 \sum_{i=1}^{3}\phi_{i,\beta}^{\mathrm{int}(K)} \\ &\quad - \sum_{\beta=1}^{k+1}\frac{2}{3}\omega_\beta\hat{\omega}_1 \left(\frac{3\Delta t}{2|K|\hat{\omega}_1} \sum_{i=1}^{3} h\big(\phi_{i,\beta}^{\mathrm{int}(K)}, \phi_{i,\beta}^{\mathrm{ext}(K)}, \boldsymbol{u}_\beta^i, \boldsymbol{x}_\beta^i, \boldsymbol{n}^i\big)|e_K^i| \right) \\ &= \sum_{\nu=1}^{M} \phi_\nu^{\mathrm{int}}\tilde{\omega}_\nu + \sum_{\beta=1}^{k+1}\frac{2}{3}\omega_\beta\hat{\omega}_1\big(H_\beta^1 + H_\beta^2 + H_\beta^3\big), \end{aligned} \tag{4.9}$$

where

$$H_\beta^1 = \phi_{1,\beta}^{\mathrm{int}(K)} - \frac{3\Delta t}{2\hat{\omega}_1|K|}\Big[h\big(\phi_{1,\beta}^{\mathrm{int}(K)}, \phi_{1,\beta}^{\mathrm{ext}(K)}, \boldsymbol{u}_\beta^1, \boldsymbol{x}_\beta^1, \boldsymbol{n}^1\big)|e_K^1| + h\big(\phi_{1,\beta}^{\mathrm{int}(K)}, \phi_{2,\beta}^{\mathrm{int}(K)}, \boldsymbol{u}_\beta^1, \boldsymbol{x}_\beta^1, -\boldsymbol{n}^1\big)|e_K^1|\Big],$$

$$\begin{aligned} H_\beta^2 = \phi_{2,\beta}^{\mathrm{int}(K)} - \frac{3\Delta t}{2\hat{\omega}_1|K|}\Big[&h\big(\phi_{2,\beta}^{\mathrm{int}(K)}, \phi_{1,\beta}^{\mathrm{int}(K)}, \boldsymbol{u}_\beta^1, \boldsymbol{x}_\beta^1, \boldsymbol{n}^1\big)|e_K^1| + h\big(\phi_{2,\beta}^{\mathrm{int}(K)}, \phi_{2,\beta}^{\mathrm{ext}(K)}, \boldsymbol{u}_\beta^2, \boldsymbol{x}_\beta^2, \boldsymbol{n}^2\big)|e_K^2| \\ &+ h\big(\phi_{2,\beta}^{\mathrm{int}(K)}, \phi_{3,\beta}^{\mathrm{int}(K)}, \boldsymbol{u}_\beta^3, \boldsymbol{x}_\beta^3, \boldsymbol{n}^3\big)|e_K^3|\Big], \end{aligned}$$

$$H_\beta^3 = \phi_{3,\beta}^{\mathrm{int}(K)} - \frac{3\Delta t}{2\hat{\omega}_1|K|}\Big[h\big(\phi_{3,\beta}^{\mathrm{int}(K)}, \phi_{2,\beta}^{\mathrm{int}(K)}, \boldsymbol{u}_\beta^3, \boldsymbol{x}_\beta^3, -\boldsymbol{n}^3\big)|e_K^3| + h\big(\phi_{3,\beta}^{\mathrm{int}(K)}, \phi_{3,\beta}^{\mathrm{ext}(K)}, \boldsymbol{u}_\beta^3, \boldsymbol{x}_\beta^3, \boldsymbol{n}^3\big)|e_K^3|\Big].$$

The term H_β^1 can be viewed as a function of $\phi_{1,\beta}^{\mathrm{int}(K)}$, $\phi_{1,\beta}^{\mathrm{ext}(K)}$ and $\phi_{2,\beta}^{\mathrm{int}(K)}$. Therefore, differentiating H_β^1 with respect to these variables and applying the CFL condition (4.8), we verify that H_β^1 is increasing in each of the arguments $\phi_{1,\beta}^{\mathrm{int}(K)}$, $\phi_{1,\beta}^{\mathrm{ext}(K)}$ and $\phi_{2,\beta}^{\mathrm{int}(K)}$. Similar arguments can be applied to H_β^2 and H_β^3. In view of equation (4.9) it follows that H is an increasing function in each of its arguments appearing in (4.7). ∎

Theorem 1 *The DG solution $\bar{\phi}_K^{n+1}$ computed from the saturation equation of (1.1) by using the DFLU numerical flux (3.37) satisfies the following maximum principle:*

$$0 \le \bar{\phi}_K^{n+1} \le 1, \tag{4.10}$$

provided the reconstructed DG polynomial $p_K(\boldsymbol{x})$ has the property that $0 \le p_K(\boldsymbol{x}) \le 1$ and that the CFL condition (4.8) is satisfied.

Proof. Lemma 5 states that the function H is increasing in each of its variable under the CFL condition (4.8).Therefore if the reconstructed DG polynomial $p_K(\boldsymbol{x})$ takes values in $[0,1]$ we get

$$H(0,\dots,0) \le \bar{\phi}_K^{n+1} \le H(1,\dots,1).$$

Hence, to prove (4.10) it suffices to show that $H(0,\dots,0) = 0$ and $H(1,\dots,1) = 1$.

Let us choose the value of the variables $\phi_{i,\beta}^{\mathrm{int}(K)}$, $\phi_{i,\beta}^{\mathrm{ext}(K)}$ and ϕ_ν^{int} equal to 1. Then we have (using the conservativity of the numerical flux)

$$H_\beta^1 = 1 - \frac{3\Delta t}{2\hat{\omega}_1|K|}\Big[h(1,1,\boldsymbol{u}_\beta^1, \boldsymbol{x}_\beta^1, \boldsymbol{n}^1)|e_K^1| + h(1,1,\boldsymbol{u}_\beta^1, \boldsymbol{x}_\beta^1, -\boldsymbol{n}^1)|e_K^1|\Big] = 1,$$

$$H_\beta^3 = 1 - \frac{3\Delta t}{2\hat{\omega}_1|K|}\Big[h(1,1,\boldsymbol{u}_\beta^3, \boldsymbol{x}_\beta^3, \boldsymbol{n}^3)|e_K^3| + h(1,1,\boldsymbol{u}_\beta^3, \boldsymbol{x}_\beta^3, -\boldsymbol{n}^3)|e_K^3|\Big] = 1,$$

$$H_\beta^2 = 1 - \frac{3\Delta t}{2\hat{\omega}_1|K|}\Big[h(1,1,\boldsymbol{u}_\beta^1, \boldsymbol{x}_\beta^1, \boldsymbol{n}^1)|e_K^1| + h(1,1,\boldsymbol{u}_\beta^2, \boldsymbol{x}_\beta^2, -\boldsymbol{n}^2)|e_K^2 + h(1,1,\boldsymbol{u}_\beta^3, \boldsymbol{x}_\beta^3, \boldsymbol{n}^3)|e_K^3|\Big].$$

Therefore

$$
\begin{aligned}
H(1,\dots,1) &= \sum_{\nu=1}^{M}\tilde{\omega}_\nu + \sum_{\beta=1}^{k+1}\frac{2}{3}\omega_\beta\hat{\omega}_1\Bigg(3 - \frac{3\Delta t}{2\hat{\omega}_1|K|}\Big[h(1,1,\boldsymbol{u}_\beta^1,\boldsymbol{x}_\beta^1,\boldsymbol{n}^1)|e_K^1| \\
&\qquad + h(1,1,\boldsymbol{u}_\beta^2,\boldsymbol{x}_\beta^2,-\boldsymbol{n}^2)|e_K^2 + h(1,1,\boldsymbol{u}_\beta^3,\boldsymbol{x}_\beta^3,\boldsymbol{n}^3)|e_K^3|\Big]\Bigg) \\
&= \sum_{\nu=1}^{M}\tilde{\omega}_\nu + \sum_{\beta=1}^{k+1}2\omega_\beta\hat{\omega}_1 - \frac{\Delta t}{|K|}\sum_{\beta=1}^{k+1}\Big[h(1,1,\boldsymbol{u}_\beta^1,\boldsymbol{x}_\beta^1,\boldsymbol{n}^1)|e_K^1| \\
&\qquad + h(1,1,\boldsymbol{u}_\beta^2,\boldsymbol{x}_\beta^2,-\boldsymbol{n}^2)|e_K^2 + h(1,1,\boldsymbol{u}_\beta^3,\boldsymbol{x}_\beta^3,\boldsymbol{n}^3)|e_K^3|\Big]\omega_\beta \\
&= 1 - \frac{\Delta t}{|K|}\sum_{i=1}^{3}\sum_{\beta=1}^{k+1}h(1,1,\boldsymbol{u}_\beta^i,\boldsymbol{x}_\beta^i,\boldsymbol{n}^i)|e_K^i|,
\end{aligned}
\tag{4.11}
$$

where we have used the equality $\sum_{\nu=1}^{M}\tilde{\omega}_\nu + \sum_{\beta=1}^{k+1}2\omega_\beta\hat{\omega}_1 = 1$, which is obtained from (4.6) if we choose the polynomial $p_K \equiv 1$.

The second term in the RHS of (4.11) indicates the quadrature rule for the flux $\mathbf{F}$, so that

$$
\begin{aligned}
\sum_{i=1}^{3}\sum_{\beta=1}^{k+1}h(1,1,\boldsymbol{u}_\beta^i,\boldsymbol{x}_\beta^i,\boldsymbol{n}^i)|e_K^i| &= \sum_{i=1}^{3}\sum_{\beta=1}^{k+1}\mathbf{F}(1,\boldsymbol{u}_\beta^i,\boldsymbol{x}_\beta^i)\cdot\boldsymbol{n}_i = \sum_{i=1}^{3}\int_{e_K^i}\mathbf{F}(1,\boldsymbol{u}_h,\boldsymbol{x})\cdot\boldsymbol{n}_i\,\mathrm{d}s \\
&= \int_{\partial K}\mathbf{F}(1,\boldsymbol{u}_h,\boldsymbol{x})\cdot\boldsymbol{n}\,\mathrm{d}s = \int_{\partial K}(\boldsymbol{u}_h + b(1)K(\boldsymbol{x})\boldsymbol{g})\cdot\boldsymbol{n}\,\mathrm{d}s \\
&= \int_K \nabla\cdot\boldsymbol{u}_h\,\mathrm{d}\boldsymbol{x} = 0,
\end{aligned}
$$

where we have used the relation $b(1) \equiv 0$ and have applied integration by parts on on the DG solution $\boldsymbol{u}_h$ in the triangle K. Thus from (4.11) we get $H(1,\dots,1) = 1$. By using a similar argument we can show that $H(0,\dots,0) = 0$, which completes the proof. ∎

Finally the maximum principle in the mean approximated solution of the saturation equation follows from the fact that the DG polynomial reconstructed with the projection map defined in §3.6 satisfies the condition $p_K(\boldsymbol{x}) \in [0,1]$ established in Theorem 1 (see [17]).

5 Numerical results

At each time step, a fixed-point method has been applied to couple of the Brinkman problem with the nonlinear transport equation. A fixed tolerance of 10^{-6} is imposed on the energy residual of each sub-problem. In addition, the involved linear systems have been solved with a preconditioned conjugate gradient method.

5.1 Example 1: Accuracy of the DFVE formulation for continuous fluxes

We start by assessing the convergence of the proposed DFVE scheme applied to a non-homogeneous version of problem (1.1) admitting the following exact solutions:

$$
\boldsymbol{u} = \sin(t)\begin{pmatrix}\sin(2\pi x_1)\cos(2\pi x_2)\\ -\cos(2\pi x_1)\sin(2\pi x_2)\end{pmatrix}, \quad p = \cos(t)\left(x_1^2 + x_2^2 - \frac{2}{3}\right), \quad \phi = \sin(t)\sin(\pi x_1)\sin(\pi x_2).
$$

The momentum equation now possesses a forcing term $\boldsymbol{r}_{\boldsymbol{u}}$ and the saturation transport equation has a nonzero right-hand side r_ϕ computed using these manufactured smooth solutions. Initial and Dirichlet boundary data are also imposed according to the exact solutions. In this test it is assumed that $\mathbf{K} = K\mathbf{I}$ is constant on Ω and the following model and stabilization parameters are

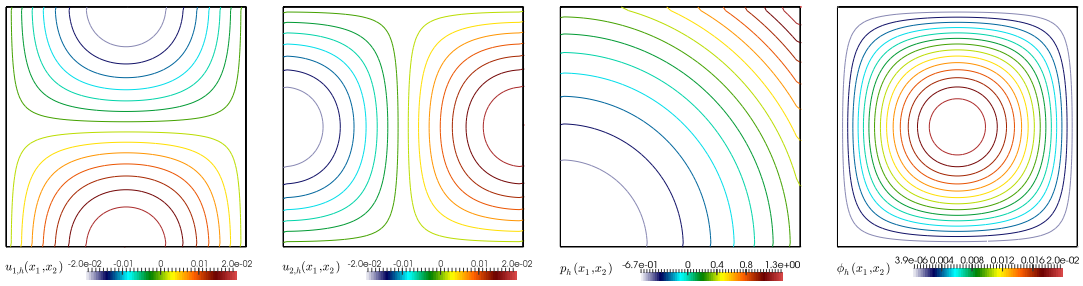

Fig. 3 Example 1: approximate solutions for the convergence test of the DFVE formulation of (1.1) with continuous flux.

h	$\mathsf{e}(\phi)$	$r(\phi)$	$\mathsf{e}(\boldsymbol{u})$	$r(\boldsymbol{u})$	$\mathsf{e}(p)$	$r(p)$
0.353553	0.016199		0.095942		0.436086	
0.282843	0.012659	1.105161	0.079099	0.865083	0.374942	0.676998
0.202031	0.008793	1.082852	0.058291	0.907209	0.285771	0.807141
0.128565	0.005449	1.058620	0.038678	0.907531	0.191638	0.884062
0.073952	0.003082	0.998464	0.021535	0.924215	0.117536	0.931678
0.039219	0.001896	0.995401	0.013448	0.970423	0.073042	0.953080

Table 1 Example 1: convergence results for the DFVE approximation of (1.1), computed on a sequence of uniformly refined partitions of $\Omega = (0,1)^2$.

adopted: $K = 10$, $\alpha_d = 1000$. Moreover, the saturation-dependent coefficients are $\mu(\phi) = (1-\frac{1}{2}\phi)^{-2}$, $f(\phi) = \phi$, $b(\phi) = \frac{1}{K}\phi^3(1-\frac{1}{2}\phi)^2$.

To study the spatial accuracy we fix a timestep $\Delta t = 0.001$, evolve the system until $T = 1$, and compute errors between the approximate and exact solutions in different norms. The obtained convergence history is displayed in Table 1.

5.2 Example 2: viscous flow on a porous square with discontinuous absolute permeability

In this test the domain coincides with the one in the previous example but we consider an heterogeneous medium composed by two different materials separated by a vertical line $x_1 = a$, and characterized by isotropic absolute permeabilities

$$\mathbf{K}(\boldsymbol{x}) = \begin{cases} \mathbf{I} & \text{if } x_1 < a, \\ 3\mathbf{I} & \text{if } x_1 > a. \end{cases}$$

In addition, the following saturation-dependent and constant coefficients are adopted:

$$K_{\mathrm{w}}(\phi) = \phi, \quad K_{\mathrm{n}}(\phi) = 1-\phi, \quad f(\phi) = \phi, \quad b(\phi) = \Delta\rho\phi(1-\phi), \quad \mu(\phi) = \mu_0(1-\phi/2)^{-\eta},$$
$$\mu_{\mathrm{w}} = \mu_{\mathrm{n}} = \phi_- = 1, \quad \boldsymbol{g} = (0,-1)^{\mathrm{T}}, \quad \eta = 2.5, \quad a = 0.5, \quad \phi_+ = 0, \quad \Delta\rho = 0.1, \quad \mu_0 = 0.01.$$

The initial saturation distribution corresponds to

$$\phi_0(\boldsymbol{x}) = \begin{cases} \phi_- & \text{if } x_1 < a, \\ \phi_+ & \text{if } x_1 > a. \end{cases}$$

On $\partial\Omega$ we assume zero-flux boundary conditions for the saturation, and slip (zero normal) velocity (see Figure 4, left). The pressure is penalized so that $p \in L^2_0(\Omega)$. At constant velocity $\boldsymbol{u} = (1,1)^{\mathrm{T}}$, the left and right branches of the flux components (denoted with $+$ and $-$ superscripts) behave as

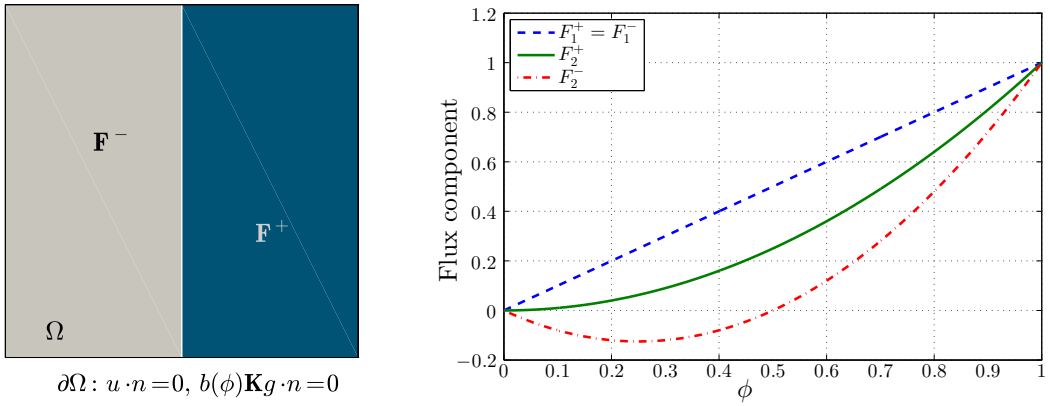

Fig. 4 Example 2: domain, material discontinuity, and boundary condition (left panel), and left and right branches of the discontinuous flux components for a constant velocity $\boldsymbol{u} = (1,1)^T$ (right).

depicted in the right panel of Figure 4. Notice that the horizontal component of the flux function is continuous for any saturation value. For this example the numerical flux is chosen as in (3.37) and the domain is discretized with 10205 points forming a primal mesh of 20408 structured triangles. A fixed timestep of $\Delta t = 0.005$ has been employed.

Initially, the interface between phases w and n is aligned with the discontinuity of the medium. Thereafter, the sharp interface ends up aligned perpendicular to the permeability discontinuity and parallel to gravity. Both pressure and velocity profiles seem to be influenced by the moving interface rather than by the domain discontinuity (see Figure 5).

5.3 Example 3: flow on a quarter-five spot with discontinuous relative and absolute permeability

We now focus on a more involved discontinuity where also the relative permeability of one phase changes from one material type to the other. The computational domain now corresponds to the upper right quarter of the well-known five spot geometry, that is, $\Omega = (0,1)^2 \setminus (B_{0.075}(0,0) \cup B_{0.075}(1,1))$, where $B_r(\boldsymbol{x}^c)$ denotes the ball of radius r centered at a given point $\boldsymbol{x}^c = (x_1^c, x_2^c)$. The domain is initially at rest and with constant saturation $\phi = \phi_0$ on the whole domain. Boundary conditions will be configured as in (2.1): an inlet section (or injector site) Γ_{in} corresponds to the bottom left corner (see the domain sketch in Figure 6), where we inject material with a low constant saturation $\phi = \phi_{\text{in}}$ at a normal inflow velocity of $\boldsymbol{u} \cdot \boldsymbol{n} = u_{\text{in}}$. At the outlet Γ_{out} (the so-called producer well, located at the top right corner of the domain) we set a constant pressure value $p = p_{\text{out}}$, whereas on the walls $\Gamma_{\text{wall}} = \partial\Omega \setminus (\Gamma_{\text{in}} \cup \Gamma_{\text{out}})$ (the remainder of the boundary), slip velocities ($\boldsymbol{u} \cdot \boldsymbol{n} = 0$) are allowed and the saturation satisfies a zero-flux boundary condition (i.e., $b(\phi)\mathbf{K}\boldsymbol{g} \cdot \boldsymbol{n} = 0$).

We choose $a, \mu(\phi), \mu_{\text{w}}, \mu_{\text{n}}$ as in the previous example. On the other hand, we impose

$$\mathbf{K}(\boldsymbol{x}) = \begin{cases} 2\mathbf{I} & \text{if } x_1 < a, \\ \mathbf{I} & \text{if } x_1 > a, \end{cases} \quad K_{\text{w}}^-(\phi) = \begin{cases} 1.75\phi & \text{if } \phi \le 0.25, \\ 0.25\phi + 0.375 & \text{if } \phi > 0.25, \end{cases} \quad K_{\text{w}}^+(\phi) = \phi,$$

$$K_{\text{n}}(\phi) = 1 - \phi^2, \quad f(\phi) = \frac{K_{\text{w}}(\phi)}{K_{\text{w}}(\phi) + K_{\text{n}}(\phi)}, \quad b(\phi) = f(\phi)K_{\text{n}}(\phi)\Delta\rho, \quad \mathbf{F}(\phi, \boldsymbol{u}) = f(\phi)\boldsymbol{u} + b(\phi)\mathbf{K}\boldsymbol{g},$$

$$\phi_{\text{in}} = 0.02, \quad \phi_0 = 0.75, \quad u_{\text{in}} = -0.1, \quad p_{\text{out}} = 2, \quad \rho_{\text{w}} = 20, \quad \rho_{\text{n}} = 10.$$

For a constant value of the velocity field we have plotted the branches of the horizontal and vertical flux components in Figure 6.

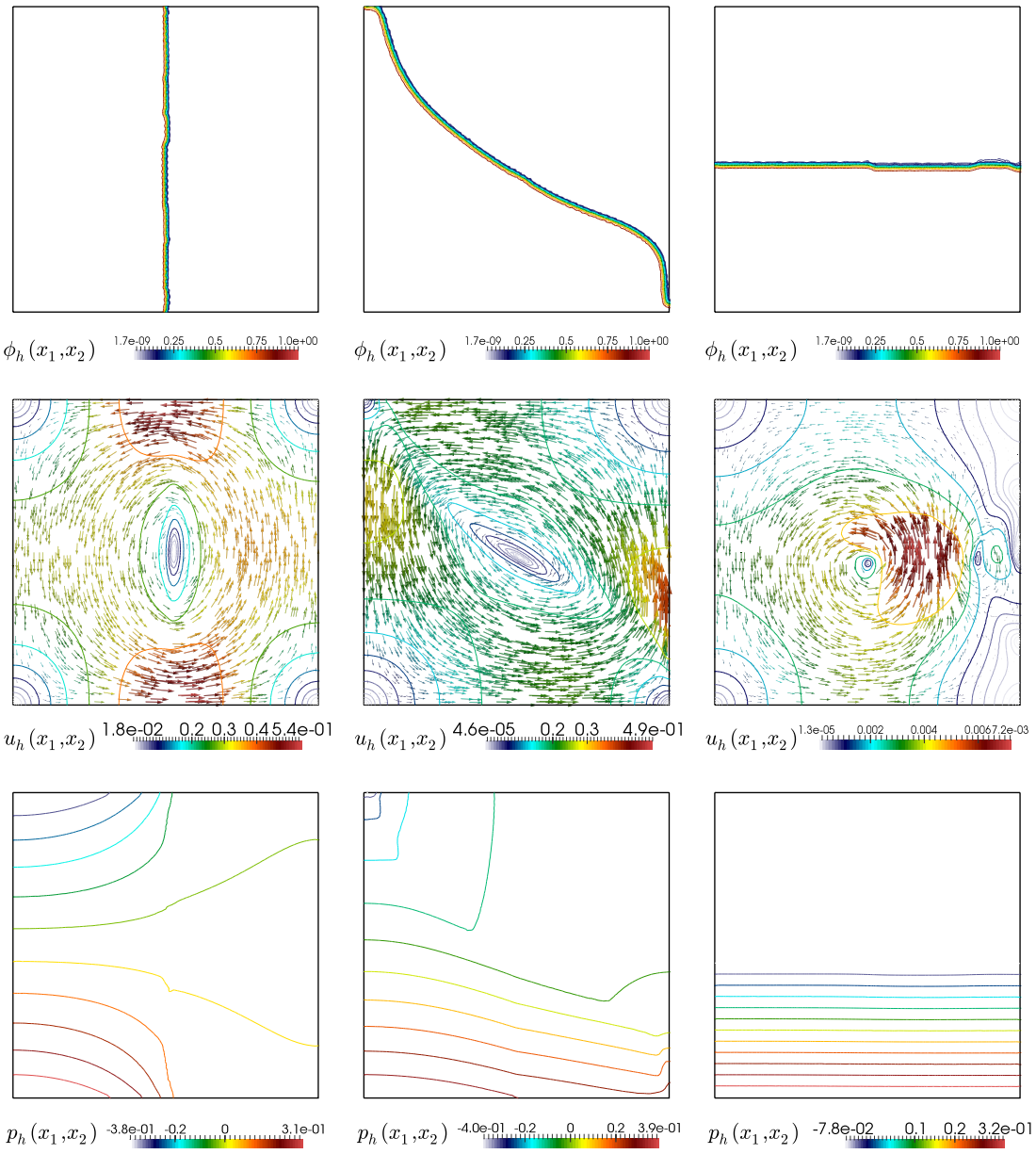

Fig. 5 Example 2: approximate saturation (top row), velocity vectors and contours of velocity magnitude (middle), and pressure contours (bottom panels), computed with the DFVE-RKDG scheme on a structured mesh of 20408 primal triangular elements, shown at early (left), middle (center), and advanced (right column) time instants.

Snapshots of the approximate saturation, velocity and pressure are portrayed in Figure 7. We observe that the low saturation fluid is flowing from the inlet towards the outlet following an unsymmetric pattern influenced by gravity and by the discontinuity of permeabilities.

5.4 Example 4

We keep the same computational domain as in Example 2 and we focus on the case of non-homogeneous absolute permeabilities, $\mathbf{K} = K(\boldsymbol{x})\mathbf{I}$, where K is given by one of the following ex-

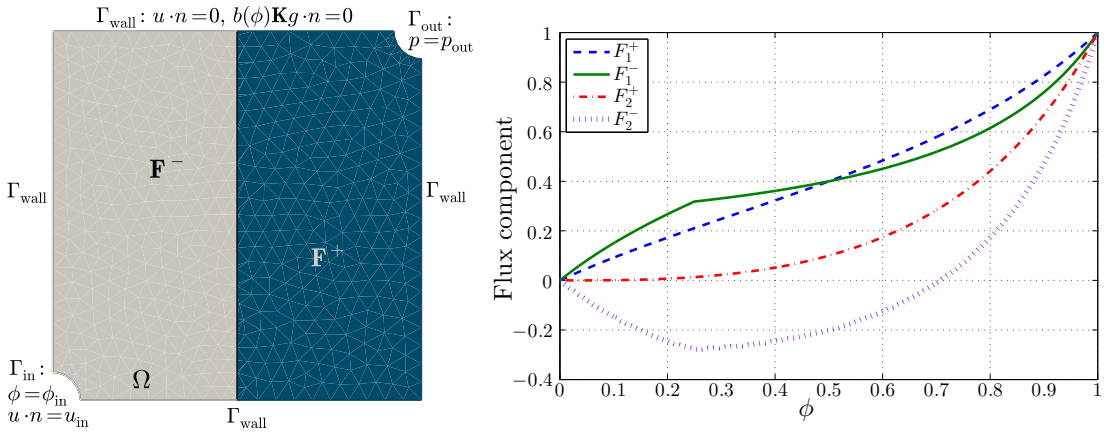

Fig. 6 Example 3: domain, flux discontinuity, and boundary configurations (left panel), and left and right branches of the discontinuous flux components for a constant velocity $\boldsymbol{u} = (1,1)^T$ (right).

pressions (see [12,28])

$$K(\boldsymbol{x}) = \begin{cases} 5.0\times 10^{-6} & \text{if } \boldsymbol{x} \in \mathrm{B}_{0.0015}(x_1^i, x_2^i) \text{ for } i \in \{1,\dots,N\}, \\ 1.5\times 10^{-5} & \text{otherwise,} \end{cases} \tag{5.1}$$

$$K(\boldsymbol{x}) = 10^{-5}\cdot \max\left\{\sum_{i=0}^{N} \boldsymbol{\Phi}_i(\boldsymbol{x}), 0.01\right\}, \quad \text{where} \quad \boldsymbol{\Phi}_i(\boldsymbol{x}) = \exp\left(-\left(\frac{|\boldsymbol{x}-\boldsymbol{x}^i|}{0.05}\right)^2\right). \tag{5.2}$$

Here $\boldsymbol{x}_i$ are 40 randomly chosen points on Ω. Moreover, the viscosities and relative permeabilities are

$$\mu_{\mathrm{w}} = 0.2, \quad \mu_{\mathrm{n}} = 1, \quad K_{\mathrm{w}}(\phi) = \phi^2, \quad K_{\mathrm{n}}(\phi) = (1-\phi)^2,$$

whereas the remaining parameters are kept as in Example 2. The fields K for both test cases are shown in Figure 8. The domain is initially at homogeneous saturation of 0.02. On the left wall we inject fluid of saturation 0.8 at an inflow velocity of 0.001. An horizontal gravity field is considered $\boldsymbol{g} = (0.0098, 0)^{\mathrm{T}}$. On the outlet (right wall) we set a zero pressure. Figure 8 also shows the approximate velocity and pressure fields at the final adimensional time $T = 500$. In addition, snapshots of the approximate saturation are collected in Figure 9. We can observe that, using the first permeability (5.1), a smooth front forms going from left to right, where saturation profiles are slightly affected by the permeability heterogeneities. On a second round we employ (5.2), which drives qualitatively different flow patterns.

6 Summary

We have presented a combined DFVE-RKDG discretization for solving two phase flow problems involving viscous porous media with discontinuous fluxes. The problem is formulated in terms of Brinkman velocity and pressure, coupled with saturation under fractional flow. An accurate Godunov-type flux reconstruction is employed along with a robust limiting procedure. Solutions obtained with the proposed scheme satisfy a discrete maximum principle. A few examples have been used to illustrate some properties of the method. Planned extensions to this work include the study of two-phase multi-component polymer flooding using the formulation introduced herein, and the sedimentation of polydisperse suspensions.

Acknowledgments. RB has been supported by Fondecyt project 1130154; BASAL project CMM, Universidad de Chile and Centro de Investigación en Ingeniería Matemática (CI^{2}MA), Universidad

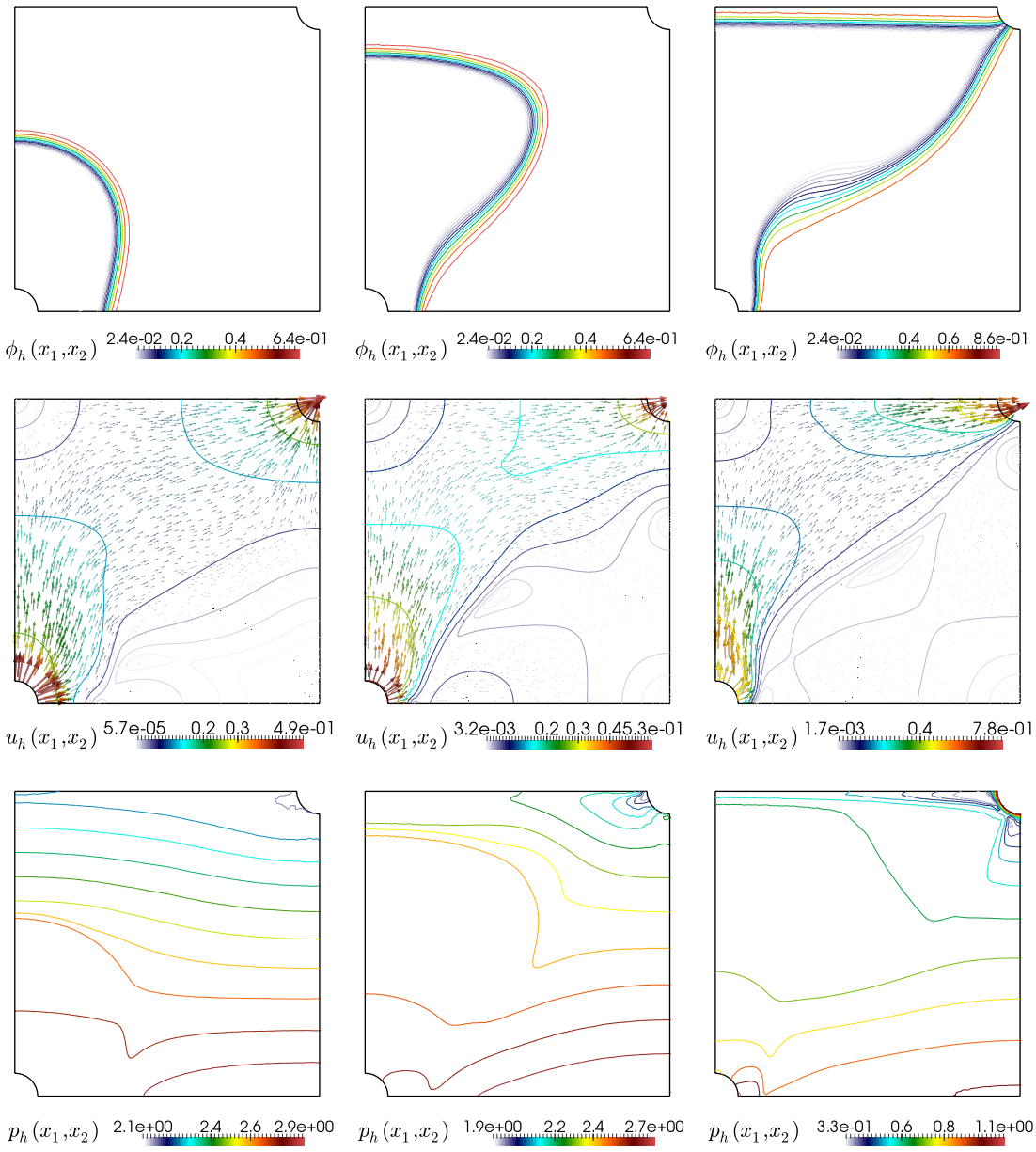

Fig. 7 Example 3: approximate saturation (top row), velocity vectors and contours of velocity magnitude (middle), and pressure contours (bottom panels), computed with the DFVE-RKDG scheme on an unstructured mesh of 7809 vertices and 15616 primal triangular elements, shown at early (left), middle (center), and advanced (right column) time instants.

de Concepción; Conicyt project Anillo ACT1118 (ANANUM); Red Doctoral REDOC.CTA, MINEDUC project UCO1202; and CRHIAM, project CONICYT/FONDAP/15130015. RRB received support by the Swiss National Science Foundation through the research grant SNSF PP00P2-144922. SKK gratefully acknowledges the financial support by the Fondecyt project 3150313.

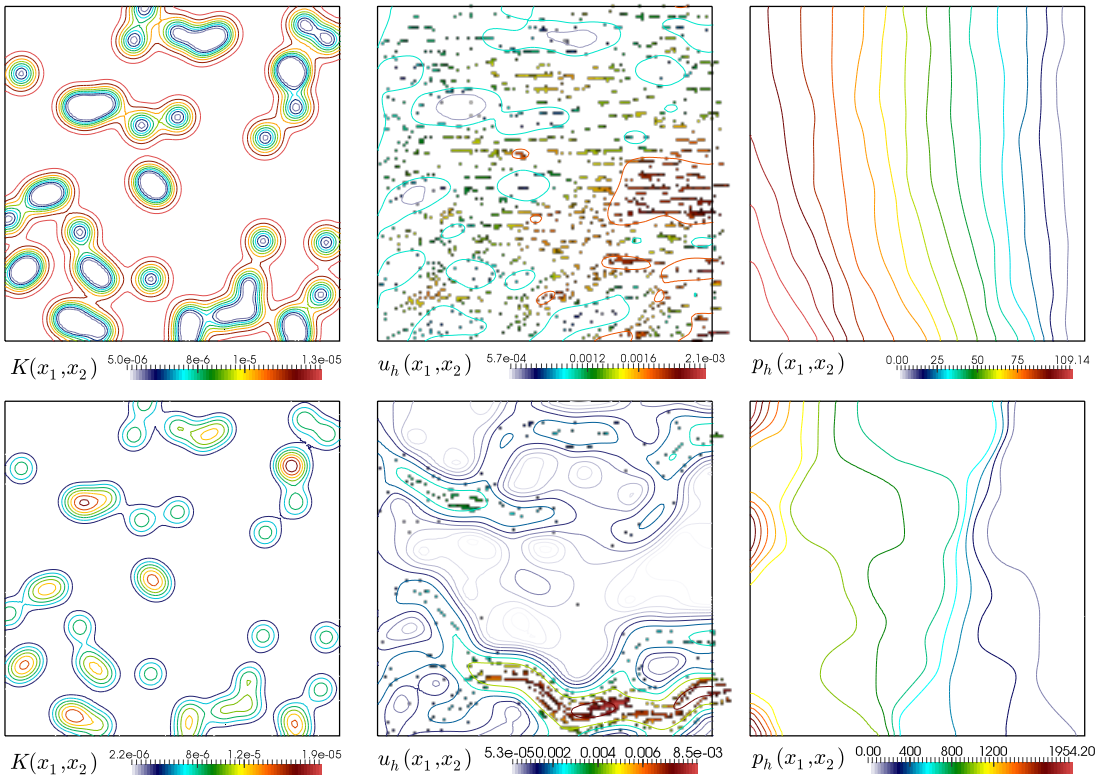

Fig. 8 Example 4: Permeability field (left column), approximate velocity vectors and magnitude contour plots (center) and pressure profiles computed at an advanced time, using (5.1) and (5.2) (top and bottom panels, respectively).

References

1. Adimurthi, J. Jaffré, G.D.V. Gowda, Godunov-type methods for conservation laws with a flux function discontinuous in space. SIAM J. Numer. Anal. (2004) 42:179–208.
2. Adimurthi, J. Jaffré, G.D.V. Gowda, The DFLU flux for systems of conservation laws. J. Comput. Appl. Math. (2013) 247:102–123.
3. V. Anaya, G.N. Gatica, D. Mora, R. Ruiz-Baier, An augmented velocity-vorticity-pressure formulation for the Brinkman problem. Int. J. Numer. Meth. Fluids (2015), in press.
4. G.E. Barter, D.L. Darmofal, Shock capturing with PDE-based artificial viscosity for DGFEM. I: formulation. J. Comput. Phys. (2010) 229(5):1810–1827.
5. P. Bastian, A fully-coupled discontinuous Galerkin method for two-phase flow in porous media with discontinuous capillary pressure. Comput. Geosci. (2014) 18:779–796.
6. C. Bi, J. Geng, Discontinuous finite volume element methods for parabolic problems. Numer. Meth. Partial Diff. Eqns. (2010) 26:367–383.
7. R. Bürger, K.H. Karlsen, H. Torres, J.D. Towers, Second-order schemes for conservation laws with discontinuous flux modelling clarifier-thickener units. Numer. Math. (2010) 116(4):579–617.
8. R. Bürger, S. Kumar, R. Ruiz-Baier, Discontinuous finite volume element discretization for coupled flow-transport problems arising in models of sedimentation. Preprint 2014-25, Centro de Investigación en Ingeniería Matemática (CI^{2}MA), Universidad de Conceopción. Available under `http://www.ci2ma.udec.cl/publicaciones/prepublicaciones/index.php`; submitted.
9. R. Bürger, R. Ruiz-Baier, K. Schneider, M. Sepúlveda, Fully adaptive multiresolution schemes for strongly degenerate parabolic equations with discontinuous flux. J. Engrg. Math. (2008) 60:365–385.
10. R. Bürger, R. Ruiz-Baier, H. Torres, A stabilized finite volume element formulation for sedimentation-consolidation processes. SIAM J. Sci. Comput. (2012) 34:B265–B289.
11. J. Camaño, R. Oyarzúa, G.N. Gatica, R. Ruiz-Baier, P. Venegas, New fully-mixed finite element methods for the Stokes-Darcy coupling. Preprint 2014-18, Centro de Investigación en Ingeniería Matemática (CI^{2}MA), Universidad de Conceopción. Available under `http://www.ci2ma.udec.cl/publicaciones/prepublicaciones/index.php`; submitted.
12. C.C. Chueh, M. Secanell, W. Bangerth, N. Djilali, Multi-level adaptive simulation of transient two-phase flow in heterogeneous porous media. Computers & Fluids (2010) 39:1585–1596.

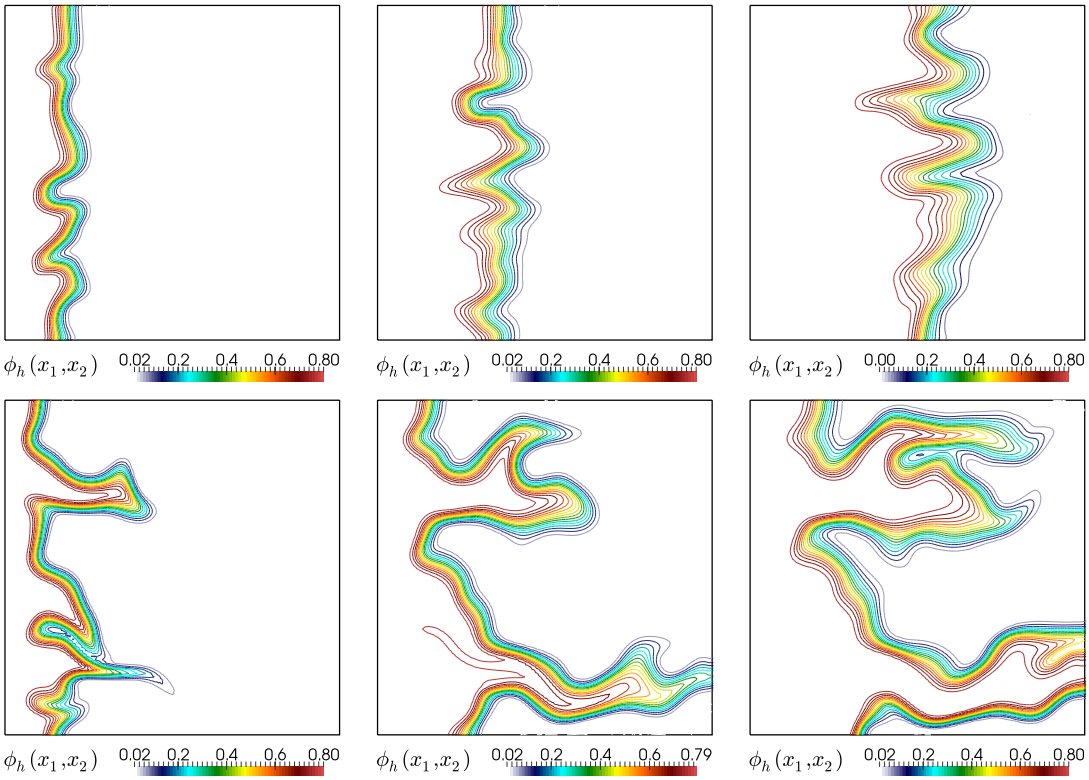

Fig. 9 Example 4: Snapshots of the saturation at early (left), middle (center), and advanced (right column) time instants using (5.1) (second row) and (5.2) (bottom row).

13. H. Class, R. Helmig, J. Niessner, U. Ölmann, Multiphase Processes in Porous Media, In: Multifield Problems in Solid and Fluid Mechanics Lecture Notes in Applied and Computational Mechanics Volume 28, 2006, pp 45–82.
14. B. Cockburn, An introduction to the discontinuous Galerkin method for convection-dominated problems, in Advanced Numerical Approximation of Nonlinear Hyperbolic Equations. Lecture Notes in Math. 1697, Springer, Berlin, 1998, pp. 151–268.
15. B. Cockburn, S. Hou, C.-W. Shu, The Runge-Kutta local projection discontinuous Galerkin finite element method for conservation laws. IV. The multidimensional case. Math. Comp. (1990) 54:545–581.
16. B. Cockburn, S.-Y. Lin, C.-W. Shu, TVB Runge-Kutta local projection discontinuous Galerkin finite element method for conservation laws III: One-dimensional systems. J. Comput. Phys. (1989) 84:90–113.
17. B. Cockburn, C.-W. Shu, The Runge-Kutta discontinuous Galerkin method for conservation laws V: Multidimensional systems. J. Comput. Phys. (1998) 141:199–224.
18. B. Cockburn, C.-W. Shu, TVB Runge-Kutta local projection discontinuous Galerkin finite element method for conservation laws II: General framework. Math. Comp. (1989) 52:411–435
19. G.M. Coclite, S. Mishra, N.H. Risebro, F. Weber, Analysis and numerical approximation of Brinkman regularization of two-phase flows in porous media. Comput. Geosci. (2014) 18(5):637–659.
20. L.J. Durlofsky, Y. Efendiev, V. Ginting, An adaptive local–global multiscale finite volume element method for two-phase flow simulations. Adv. Water Res. (2007) 30(3):576–588.
21. P. Frolkovič, H. De Schepper, Numerical modelling of convection dominated transport coupled with density driven flow in porous media. Adv. Water Res. (2001) 24:63–72.
22. A. Fumagalli, A. Scotti, A numerical method for two-phase flow in fractured porous media with non-matching grids. Adv. Water Res. (2013) 62(C):454–464.
23. F. Furtado, V. Ginting, F. Pereira, M. Presho, Operator splitting multiscale finite volume element method for two-phase flow with capillary pressure. Transp. Porous Med. (2011) 90:927–947.
24. W. Jäger, A. Mikelic, On the interface boundary condition of Beavers, Joseph and Saffmann. SIAM J. Appl. Math. (2000) 60:1111–1127.
25. S. Kumar, A mixed and discontinuous Galerkin finite volume element method for incompressible miscible displacement problems in porous media. Numer. Meth. Partial Diff. Eqns. (2012) 28:1354–1381.
26. S. Kumar, N. Nataraj, A.K. Pani, Discontinuous Galerkin finite volume element methods for second order linear elliptic problems. Numer. Meth. Part. Diff. Eqns. (2009) 25:1402–1424.
27. S. Kumar, R. Ruiz-Baier, Equal order discontinuous finite volume elements for the Stokes problem. J. Sci. Comput. (2015), in press. DOI:10.1007/s10915-015-9993-7

28. K. Sudarshan Kumar, C. Praveen, G.D.V. Gowda, A finite volume method for a two-phase multicomponent polymer flooding. J. Comput. Phys. (2014) 275:667–695.
29. R.D. Lazarov, S.Z. Tomov, Adaptive finite volume element method for convection-diffusion-reaction problems in 3-D. In: P. Minev, Y. Lin (Eds.), Scientific Computing and Applications, Nova Sci. Publish. Inc., NY, USA (2001), pp. 91–106.
30. Z. Luo, H. Li, P. Sun, A fully discrete stabilized mixed finite volume element formulation for the non-stationary conduction-convection problem. J. Math. Anal. Appl. (2013) 404:71–85.
31. R. Rannacher and S. Turek, Simple nonconforming quadrilateral Stokes element. Numer. Meth. Partial Diff. Eqns. (1992) 8:97–111.
32. R. Ruiz-Baier, I. Lunati, Mixed finite element – primal finite volume element discretization of multicontinua flow models, (2015) submitted.
33. R. Ruiz-Baier, H. Torres, Numerical solution of a multidimensional sedimentation problem using finite volume-elements, Appl. Numer. Math. (2015), in press. DOI:10.1016/j.apnum.2013.12.006
34. M.F. Wheeler, T. Wick, W. Wollner, An augmented-Lagrangian method for the phase-field approach for pressurized fractures. Comp. Meth. Appl. Mech. Engrg. (2014) 271:69–85.
35. Z.L. Xu, X.-Y. Chen, Y.J. Liu, A New Runge-Kutta discontinuous Galerkin method with conservation constraint to improve CFL condition for solving conservation laws. J. Comput. Phys. (2014) 278:348–377.
36. X. Ye, A discontinuous finite volume method for the Stokes problem. SIAM J. Numer. Anal. (2006) 44:183–198.
37. X. Zhang, Y. Xia, C.-W. Shu, Maximum-principle-satisfying and positivity-preserving high order discontinuous Galerkin schemes for conservation laws on triangular meshes. J. Sci. Comput. (2012) 50:29-62.